Universität Münster

Marian Fritz Baade

› Performance Study of the babyMOSS Pixel Sensor in a Test Beam at ELSA

2026

living.knowledge



Performance Study of the babyMOSS Pixel Sensor in a Test Beam at ELSA

Bachelor thesis
submitted to the

Universität Münster
Institut für Kernphysik

by

Marian Fritz Baade

February 2026

First examiner:	Anton Andronic
Second examiner:	Christian Klein-Bösing
Day of submission:	Sunday 15th February, 2026

Declaration of Academic Integrity

I hereby confirm that this thesis, entitled *Performance Study of the babyMOSS Pixel Sensor in a Test Beam at ELSA*, is solely my own work and that I have used no sources or aids other than the ones stated. All passages in my thesis for which other sources, including electronic media, have been used, be it direct quotes or content references, have been acknowledged as such and the sources cited. I am aware that plagiarism is considered an act of deception which can result in sanction in accordance with the examination regulations.

I consent having my thesis cross-checked with other texts to identify possible similarities and to having it stored in a database for this purpose.

I confirm that I have not submitted the following thesis in part or whole as an examination paper before.

Münster, 15th February 2026



Marian Fritz Baade

Contents

List of Acronyms **vii**

1 Introduction **1**

2 Theoretical Background **3**
2.1 Interaction of Charged Particles with Matter 3
2.2 Semiconductor Particle Detectors 4
2.2.1 Semiconductor Fundamentals 4
2.2.2 Formation of the pn-Junction 6
2.2.3 Signal Generation 7
2.3 Monolithic Active Pixel Sensors 7
2.4 Tracking in a Beam Telescope 9
2.4.1 Track Reconstruction Algorithms 10
2.4.2 Detection Efficiency 11
2.4.3 Spatial Resolution 11

3 ALICE at the LHC **13**
3.1 The Inner Tracking System (ITS)3 Upgrade 14
3.2 The MOSS and babyMOSS Prototypes 15

4 Experimental Methods – Beam Telescope **19**
4.1 Raiser-DAQ and Beam Telescope Setup 20
4.2 Trigger Chain 22
4.3 Test Beam Facility (ELSA) 23
4.4 Data Taking and Acquisition 25
4.5 Data Analysis with Corryvreckan 28
4.5.1 Masking 29
4.5.2 Clustering 30
4.5.3 Prealignment 30

4.5.4 Alignment 31

5 Analysis **33**
5.1 Raw Hitmaps and Beam Position 34
5.2 Detection Efficiency 38
5.3 Spatial Resolution 41
5.4 Track Quality and Selection 46

6 Summary and Outlook **49**

A Additional Figures and Tables **51**
A.1 Detection Efficiency 53
A.2 Spatial Resolution 57
A.3 FHR and THR scans 61

List of Figures **67**

List of Tables **71**

Bibliography **73**

List of Acronyms

DUT Device Under Test

MAPS Monolithic Active Pixel Sensors

FHR Fake Hit Rate

THR Threshold

ITS Inner Tracking System

ALICE A Large Ion Collider Experiment

LHC Large Hardon Collider

CERN European Organization for Nuclear Research

QGP Quark-Gluon Plasma

MOSS Monolithic Stitched Sensor

babyMOSS baby Monolithic Stitched Sensor

CMOS Complementary Metal-Oxide-Semiconductor

GBL General Broken Lines

LHCb Large Hadron Collider beauty

CMS Compact Muon Solenoid

ATLAS A Toroidal LHC Apparatus

TPC Time Projection Chamber

RSU Repeated Sensor Unit

HU Half Unit

FPGA Field-Programmable Gate Array

PCB Printed-Circuit Board

QCD Quantum Chromodynamics

LINAC Linear Accelerator

ELSA Electron Stretcher Facility

DAQ Data Acquisition

PMT Photomultiplier Tube

SSH Secure Shell

1 Introduction

Understanding the fundamental constituents of matter and the forces governing their interactions requires recreating, as closely as possible, the extreme conditions that existed in the very early universe. High-energy particle collisions provide a controlled environment to probe these regimes and to study phenomena that cannot be accessed under ordinary laboratory conditions. Over the past decades, major advances in this field have been achieved at the A Large Ion Collider Experiment (ALICE) at the European Organization for Nuclear Research (CERN).

ALICE is one of the four key experiments at the Large Hardon Collider (LHC) and is dedicated to the study of strongly interacting matter at extreme temperature and density. It focuses on ultra-relativistic heavy-ion collisions to explore the properties of the Quark-Gluon Plasma (QGP), a deconfined phase of quarks and gluons that is expected to have existed during the first microseconds after the Big Bang. The study of this state of matter provides essential insights into Quantum Chromodynamics in the non-perturbative regime [1, pp. 1-2].

To access these physics goals, ALICE relies on precise tracking and particle identification in an environment with high particle multiplicity. This places stringent requirements on the performance of the tracking detectors, especially close to the interaction point, where excellent spatial resolution and a minimal material budget are essential [2, p. 7].

Continuous advances in detector technology therefore play a crucial role in the ALICE physics program. In this context, ALICEs ITS is undergoing a major upgrade towards a new generation of ultra-thin, monolithic silicon pixel detectors, designed to further improve vertexing and tracking performance [3, p. 3].

Within the ITS3 research and development program several prototype sensors have been developed; one of the these is the *babyMOSS*. This thesis will focus on investigating the performance of the babyMOSS in terms of detection efficiency and spatial resolution as a function of particle rate in the range from 1 kHz to 15 kHz.

The measurements were carried out at the ELSA test-beam facility in Bonn and represent, to the author's knowledge, one of the first studies performed at this facility with dynamically varying beam rates.

Theoretical Background

2

This chapter provides an overview of the fundamental physical concepts required for the understanding of this thesis. The theoretical background and detector concepts presented in this chapter are largely based on the textbook by Kolanoski and Wermes [4]. The relevant theories represented in the chapter range from the interaction of charged particles with matter as well as the basics of semiconductor detectors, especially pixel sensors, to the concept of tracking and used quantities for the characterization of such sensors.

2.1 Interaction of Charged Particles with Matter

When charged particles traverse matter, the interactions between matter and particle results in energy loss of the particles. The main constituent of these losses are the ionization and excitement of the electrons in the target atoms. The mean energy loss of heavy charged particles is commonly described by the Bethe-Bloch formalism [5]

$$\left\langle -\frac{dE}{dx} \right\rangle = 4\pi N_A r_e m_e c^2 \frac{z^2 Z}{A} \frac{1}{\beta^2} \left[\frac{1}{2} \ln\left(\frac{2m_e c^2 \beta^2 \gamma^2 W_{\max}}{I^2} \right) - \beta^2 - \frac{\delta(\beta\gamma)}{2} \right], \quad (2.1)$$

where z is the charge number of the incident particle, Z and A are the atomic number and mass number of the absorber material. N_A is the Avogadro's constant, while r_e and m_e denote the classical radius and the mass of an electron. The relativistic parameters are defined as $\beta = v/c$ and $\gamma = 1/\sqrt{1 - v^2/c^2}$ with c as the speed of light. The term $W_{\max}$ represents the maximum kinetic energy that can be transferred in a single collision, while I is the mean excitation energy of the absorber material. The correction term $\delta(\beta\gamma)$ accounts for density effects.

The Bethe–Bloch formula is valid for heavy charged particles in the approximate range $0.1 \leq \beta\gamma \leq 1000$. The energy loss of electrons an positrons, hence their

small mass, is not covered by the formula. Additional interaction processes as the bremsstrahlung must be considered [4, 5].

2.2 Semiconductor Particle Detectors

Semiconductors form the physical basis of solid-state radiation detectors and are characterized by a crystalline structure that causes distinct electronic properties. In contrast to metals and insulators, semiconductors have an finite energy gap between occupied and unoccupied electronic states, which allows their electrical behavior to be controlled by material composition and external fields. These properties are essential for the generation and collection of charge carriers in particle detectors. In the following, the fundamental semiconductor concepts relevant for detector operation are introduced, with focus on crystalline silicon [4].

2.2.1 Semiconductor Fundamentals

Semiconductor detector materials are crystalline solids with a periodic atomic lattice. Silicon crystallizes in a diamond cubic structure, in which each atom is covalently bonded to its four nearest neighbors. This regular arrangement leads to the formation of so called energy bands. The two highest bands are the valence and conduction band.

The valence band contains the electronic states associated with covalent bonding, while the conduction band consists of higher-energy states in which electrons can move freely through the crystal. These two bands are separated by an energy gap in which no allowed electronic states exist. The presence of this band gap is the defining feature of a semiconductor and determines its electrical properties. When there are no external perturbations, electrons occupy the lowest available energy states. Electrical conduction becomes possible only if electrons are lifted into the conduction band, leaving behind vacancies in the valence band. These vacancies behave as positively charged mobile carriers, referred to as holes. Both electrons and holes contribute to charge transport under the influence of an electric field. In silicon the band gap at $300\,\mathrm{K}$ is sufficiently small ($E_g = 1.12\,\mathrm{eV}$), that thermal excitation enables the promotion of electrons. In an isolator on the other hand the band gap is comparatively large ($E_g \approx 9$ eV), making a transfer by thermal excitation and with that conductivity very unlikely. For conductors (like most metals) this is not the case, as they have overlapping valence and conduction bands or a

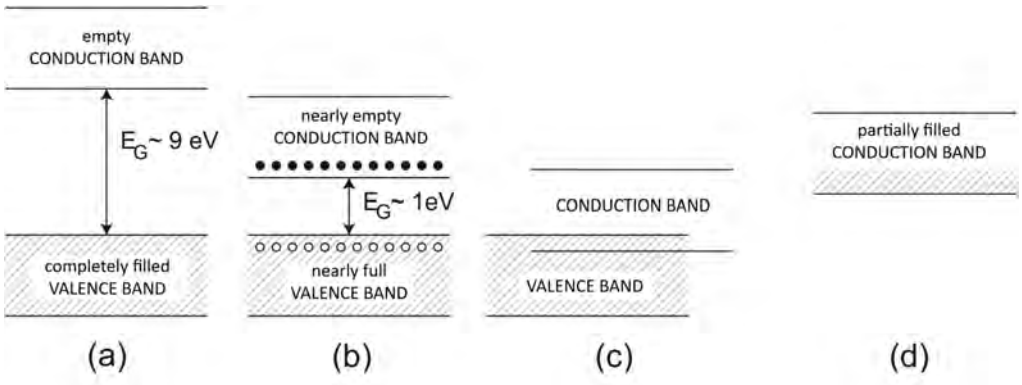


Figure 2.1: Schematical representation of energy band structure of isolators (a), semiconductors (b) and conductors (c,d). E_g is the width of the band gap in terms of energy. Taken and translated from [4, p. 278].

partially filled conduction band, making current conduction possible with the least amount of energy input. The concept of energy bands and an comparison between isolators, semiconductors and conductors is given schematically in figure 2.1 [4, pp. 277–279].

For detector applications, the electrical properties of semiconductors are modified by the intentional introduction of impurity atoms into the crystal lattice. This process, known as doping, creates additional energy levels within the band gap and allows control over the type and density of mobile charge carriers. There are two types of impurities:

1. Donor impurities possess one more valence electron than the host material. When incorporated into the lattice, they form weakly bound electronic states close to the conduction band. Electrons that are occupying these so called donor levels can be released into the conduction band with relatively little energy. As a result, electrons become the dominant mobile charge carriers, and the material is referred to as n-type.

2. Acceptor impurities, on the other hand, have one fewer valence electron than the host atoms. They introduce energy levels near the valence band that can capture electrons from the valence band, leaving behind mobile holes. In this case, holes dominate charge transport, and the material is p-type.

In silicon, acceptor dopants such as boron produce p-type material, while donor dopants such as arsenic result in n-type conductivity. The band gap remains essentially unchanged, but the concentration of mobile charge carriers is modified. For detector applications, the dopant concentration and spatial distribution are essential, as they determine the formation of internal electric fields and thereby the charge transport and collection within the device [4, pp. 285–288].

2.2.2 Formation of the pn-Junction

A key element of semiconductor detector technology is the pn-junction, which is formed when p-type and n-type semiconductor regions are brought into contact. Due to the concentration gradients at the interface, electrons from the n-type region and holes from the p-type region diffuse across the junction. This diffusion leads to recombination of charge carriers near the interface and leaves behind ionized donor and acceptor atoms in the lattice. As mobile charge carriers diffuse across the junction and partially recombine near the interface, ionized acceptor atoms on the p-type side and ionized donor atoms on the n-type side remain fixed in the crystal lattice. This results in a negative space-charge density in the p-type region and a positive space-charge density in the n-type region. The region containing these immobile charges is known as the depletion region. The associated charge separation gives rise to an internal electric field that counteracts further diffusion of carriers and establishes an equilibrium across the junction. The structure of a pn-junction with the corresponding densities and the electric field is illustrated in figure 2.2.

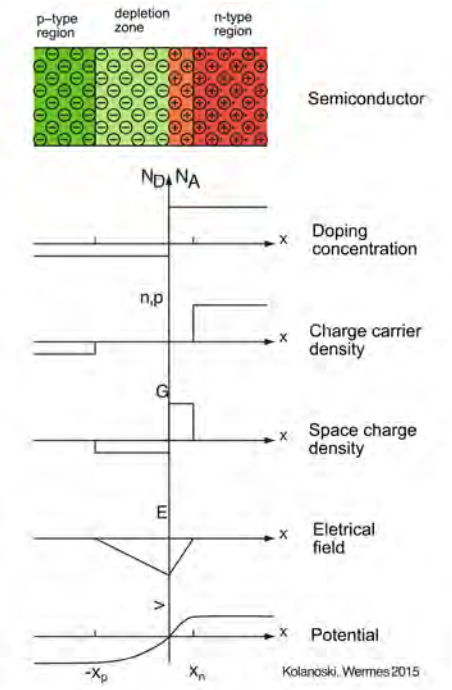


Figure 2.2: Schematic illustration of a pn-junction, showing the depletion region and the internal electric field. Taken and modified from [4].

When an external voltage is applied, the width of the depletion region changes depending on the polarity of the bias. Under reverse bias, corresponding to a positive

potential at the n-type side and a negative potential at the p-type side, the depletion region widens and the electric field strength increases. For detector operation, the pn-junction is therefore typically operated under reverse bias to maximize the depleted volume. The extent of the depletion region depends on the applied voltage as well as on the doping concentrations of the p-type and n-type regions [4, pp. 288–293].

2.2.3 Signal Generation

The signal in a silicon detector is generated when a charged particle traverses the depleted volume and loses energy through inelastic interactions with the atomic electrons of the material. These interactions lead mainly to ionization, resulting in the creation of electron hole pairs along the particle trajectory. In silicon, the average energy required to produce one electron hole pair is approximately $w = 3.6\,\mathrm{eV}$, which is larger than the band gap due to additional energy transfer to lattice excitations [4, pp. 292–294]. The total charge generated in the sensitive volume is therefore proportional to the deposited energy and can be expressed as

$$Q = \frac{E}{w}\, e, \tag{2.2}$$

where E denotes the energy deposited in the silicon sensor and e is the elementary charge [6, p. 11]. In thin silicon sensors, such as those used in pixel detectors, the energy deposited by a single traversing particle is small and subject to large statistical fluctuations. The resulting charge deposition follows a Landau-like distribution rather than the mean energy loss. The generated electron hole pairs are subsequently separated by the electric field in the depleted region and collected at the electrodes, giving rise to a measurable electrical signal. A detailed discussion of signal formation and charge deposition in thin silicon detectors can be found in [6, pp. 28–35].

2.3 Monolithic Active Pixel Sensors

Monolithic Active Pixel Sensors (MAPS) integrate the sensitive volume and the readout electronics within a single silicon substrate, in contrast to hybrid pixel detector concepts based on separate sensor and readout chips. The use of Complementary

Metal-Oxide-Semiconductor (CMOS) technology allows the implementation of complex in-pixel circuitry, including amplification, discrimination, and digital logic, directly within the sensor. As a result, MAPS provide a fully digital output without the need for an external readout chip. This high level of integration significantly reduces the material budget and simplifies detector assembly, which is a big advantage for vertex detectors where multiple scattering must be minimized.

As a representative example of a modern MAPS, the *ALPIDE* sensor, developed for the ALICE ITS 2, is briefly introduced to illustrate the pixel cross-section and charge collection concept. A schematic cross-sectional view of an *ALPIDE* sensor pixel is shown in figure 2.3. The sensor features a layered structure consisting of a highly p^+-doped substrate, and a weakly p^--doped epitaxial layer whose doping concentration is several orders of magnitude lower. This configuration enables efficient charge collection while reducing recombination losses.

The epitaxial layer contains several CMOS implants, such as p-wells and n-wells, which form the basis of the in-pixel readout circuitry. These implants are electrically isolated from the epitaxial layer by a deep p-well in order to prevent the n-wells of the CMOS transistors from acting as parasitic charge collection nodes. Charge collection is instead performed by a dedicated n-well implant located at the center of each pixel [7, pp. 41–43].

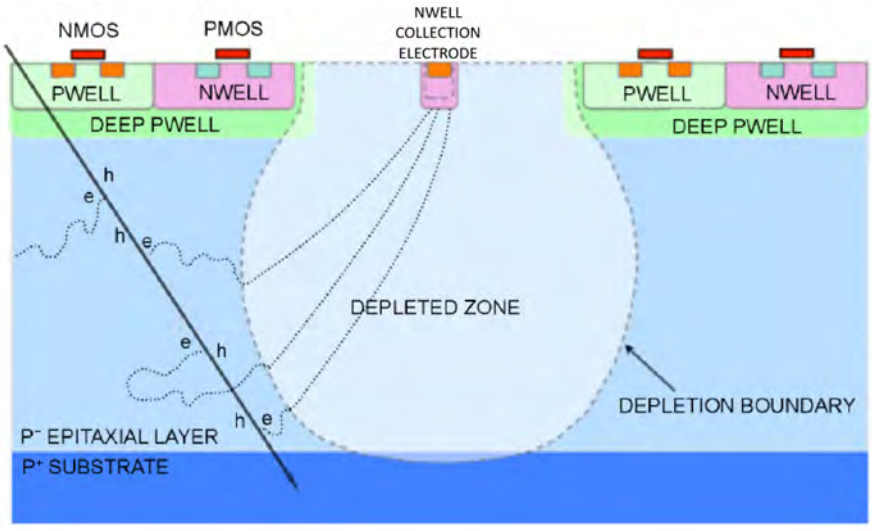


Figure 2.3: Schematic visualization of the *ALPIDE* cross section. Taken and adapted from [7].

When a charged particle traverses the epitaxial layer, electron hole pairs are generated. The charge carriers primarily propagate by diffusion towards the depleted region surrounding the collection electrode, where they are then transported by drift. Similar to a conventional pn junction, the size of the depletion region can be increased by applying a reverse bias voltage to the substrate, improving charge collection efficiency and timing [7, p. 43].

Recent generations of MAPS produced in advanced CMOS technologies, such as the 65 nm process, enable small pixel pitches and reduced collection electrode sizes. This leads to improved spatial resolution, typically of the order of a few micrometers, and reduced sensor capacitance. The lower power consumption associated with these designs allows for air cooling in many applications, further contributing to a reduced material budget[7, 2].

In MAPS pixel detectors, charge carriers generated by a traversing particle can spread laterally in the weakly doped epitaxial layer due to diffusion before being collected by the electrodes. This leads to charge sharing among neighbouring pixels and to the reconstruction of particle hits as clusters of adjacent pixels. Cluster formation is essential to achieve a spatial resolution higher than the binary resolution limit (see section 2.4.3) [7].

2.4 Tracking in a Beam Telescope

Beam telescopes provide a reference system for the characterization of prototype detectors in test beam experiments. A detailed description of a beam telescope is presented in section 4.1. By determining the trajectories of charged particles with several reference detectors, the expected hit position on a Device Under Test (DUT) can be determined and compared to the actual hit position on the DUT. This enables the extraction of intrinsic detector performance parameters such as detection efficiency and spatial resolution [8, p. 1–3].

The achievable precision of the reconstructed track is limited by the spatial resolution of the reference planes, their geometrical configuration, and the amount of material traversed by the particle. In particular, multiple Coulomb scattering introduces deviations from an ideal straight trajectory and limits the accuracy of track reconstruction in beam telescope setups. Multiple Coulomb scattering is caused by elastic interactions of the charged particle with atomic nuclei in the detector

material. The characteristic width of the resulting angular distribution can be approximated by the Highland formula [4, p. 73],

$$\theta_0 \simeq \frac{13.6\,\mathrm{MeV}}{\beta pc}\, z \sqrt{\frac{x}{X_0}} \left[1 + 0.038 \ln\left(\frac{x}{X_0}\right)\right], \tag{2.3}$$

where p is the particle momentum, βc its velocity, z the particle charge, x the thickness of the traversed material, and X_0 the radiation length.

For charged particles with $\beta \simeq 1$ this approximation of θ_0 is accurate to about 11% for $10^{-3} < x/X_0 < 100$ [5, p. 403]. This approximation is therefore well suited for the description of multiple scattering effects in most beam telescope configurations. To improve the quality of the track reconstruction and account for these deviations the applied tracking algorithm is of importance.

2.4.1 Track Reconstruction Algorithms

Several tracking approaches are commonly employed to account for multiple scattering. Local, sequential methods such as the Kalman filter combine pattern recognition and track fitting by reconstructing a single track from a starting point typically at the end of a trajectory. The algorithm predicts the region in which the next hit is expected. This process continues through the detector planes and updates the fit parameters with every compatible measurements. Random perturbations of the trajectory, most notably multiple scattering, are incorporated as process noise in the fit. Further information on the topic are found in [9, 10].

Alternatively, global fitting methods such as the General Broken Lines (GBL) algorithm describe the particle trajectory as a sequence of linear segments connected by discrete scatter points. The scattering angles at these points are treated as fit parameters, and all measurements and scattering contributions are included simultaneously in a global least-squares minimization, yielding an optimal estimate of the track parameters [11].

In practical beam telescope analyses, it is common to use a Kalman filter to obtain an initial track estimate and subsequently refine the result using a GBL fit. This combination exploits the computational efficiency of the Kalman filter while benefiting from the accuracy of a global fit [8, p. 7–11].

2.4.2 Detection Efficiency

The detection efficiency ε describes the probability that a charged particle traversing the detector is successfully detected and reconstructed as a hit. In beam telescope measurements, it is defined as the ratio of the number of reconstructed reference tracks with an associated cluster in the DUT, N_{assoc}, to the total number of selected reference tracks, N_{trk} [8, p. 8–9],

$$\varepsilon = \frac{N_{\text{assoc}}}{N_{\text{trk}}}. \tag{2.4}$$

The detection efficiency not only represents the performance of the sensor, but also is dependent on the setup the sensor is operated with and the analysis carried out to obtain the efficiency values [8].

2.4.3 Spatial Resolution

For a purely binary readout with a uniform hit probability across a pixel of pitch p, the intrinsic spatial resolution is given by

$$\sigma_{\text{bin}} = \frac{p}{\sqrt{12}}. \tag{2.5}$$

This value represents the resolution limit of an ideal digital pixel detector and is commonly used as a reference when interpreting measured spatial resolutions [4, pp. 842-843].

In beam telescope measurements, the spatial resolution of the DUT is determined from the distribution of residuals, defined as the difference between the hit position measured in the DUT and the position predicted by the reconstructed reference track in a given spatial direction:

$$r = x_{\text{hit}} - x_{\text{track}}. \tag{2.6}$$

For a Gaussian residual distribution the standard deviation is given by

$$\sigma_{\text{res}}^2 = \sigma_{\text{DUT}}^2 + \sigma_{\text{track}}^2, \tag{2.7}$$

where σ_{DUT} denotes the intrinsic spatial resolution of the DUT and σ_{track} the track resolution at the DUT position. The intrinsic detector resolution can therefore be obtained by subtracting the track resolution in quadrature [8, pp. 8–9].

3 ALICE at the LHC

ALICE is one of the four major experiments operating at the LHC at the CERN. The LHC is a circular synchrotron with a circumference of 27.7 km and represents the final stage of the CERN accelerator complex. It accelerates and collides protons as well as heavy ions, in particular lead nuclei, reaching center-of-mass energies of $\sqrt{s_{\mathrm{NN}}} = 13.6\ \mathrm{TeV}$ for proton–proton collisions and $\sqrt{s_{\mathrm{NN}}} \approx 5\ \mathrm{TeV}$ per nucleon pair for Pb–Pb collisions during Run 3 [7, p. 2].
The colliding beams are generated and pre-accelerated in a chain of linear accelerators and synchrotrons before being injected into the LHC ring at an energy of $450\,\mathrm{GeV}$, where they are further accelerated to their final energy. Two counter-rotating beams circulate in separate beam pipes and intersect at four interaction points, which host the experiments A Toroidal LHC Apparatus (ATLAS) [12], Compact Muon Solenoid (CMS) [13], Large Hadron Collider beauty (LHCb) [14], and A Large Ion Collider Experiment (ALICE) [15]. While ATLAS and CMS are designed as general-purpose detectors and LHCb focuses on heavy-flavour physics, ALICE is uniquely optimized for the study of ultra-relativistic heavy-ion collisions [7, pp. 2–3].

The primary physics goal of ALICE is the investigation of strongly interacting matter under extreme conditions, as described by Quantum Chromodynamics (QCD). In particular, ALICE aims to study the properties of the QGP, a deconfined state of quarks and gluons expected to form at very high energy densities and temperatures [1, pp. 1-3] To access this regime, ALICE performs measurements not only in proton–proton collisions but also in proton–ion and ion–ion collisions, with a strong emphasis on Pb–Pb systems. These physics objectives impose stringent requirements on the detector design, as heavy-ion collisions at the LHC produce extremely high particle multiplicities. The ALICE detector is therefore optimized to operate at interaction rates of up to $50\,\mathrm{kHz}$ in Run 3 while maintaining excellent tracking and particle-identification capabilities down to very low transverse momenta [2, pp. 9–11]. A schematic overview of the detector is shown in Fig. 3.1.

The central barrel is embedded in a solenoidal magnetic field and hosts the main tracking detectors, most notably the ITS and the Time Projection Chamber (TPC). Together, these detectors enable precise reconstruction of charged-particle trajectories and momenta, as well as particle identification using complementary measurement techniques [16, pp. 5–6].

The tracking performance of ALICE is largely defined by the detector layers closest to the interaction point. These measurements are provided by the Inner Tracking System, which is therefore a key component of the experiment [7, pp. 8–9]. To further improve its performance, a new generation of silicon pixel detectors is being developed within the ITS3 upgrade.

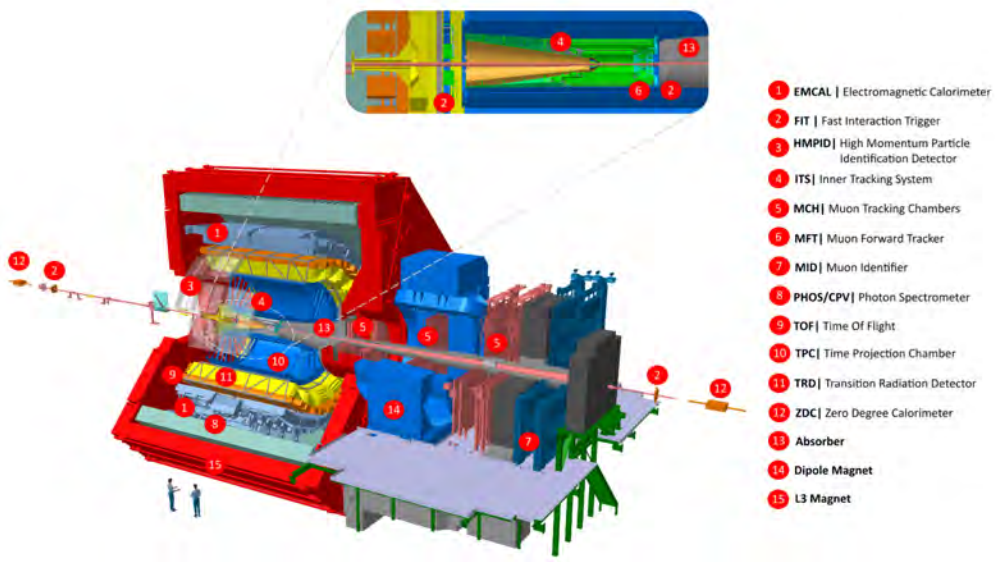


Figure 3.1: Schematic overview of the ALICE 2 detector and its main subdetectors. Taken from [16]

3.1 The ITS3 Upgrade

During the Long Shutdown 3 (2026-2029), the ALICE Inner Tracking System will undergo a major upgrade, referred to as ITS3. The aim of this upgrade is to significantly improve vertexing and tracking performance by replacing the three innermost layers of the current ITS2 with a new generation of ultra-thin MAPS [2].

The present ITS2 is based on the *ALPIDE* sensor, produced in a 180 nm CMOS imaging process with a pixel pitch of $28\ \mu\mathrm{m} \times 28\ \mu\mathrm{m}$. For the ITS3, a MAPS design

based on a 65 nm CMOS imaging process is being developed. This transition allows for smaller in-pixel circuitry, improved charge-collection properties and the production on larger 300 mm wafers [2].

An important feature is the use of wafer-scale sensors, overcoming reticle-sized limitations by stitching and realizing a sensor length of $259\ \mathrm{mm}$ and a thinness of approximately $50\ \mu\mathrm{m}$. This enables the sensors to be mechanically bent and arranged in a truly cylindrical geometry around the beam pipe with an distance of 2 mm, thereby reducing the material budget to 0.07 % X_0. The readout electronics and power distribution are shifted to dedicated end-cap regions on the sides of the sensor, further reducing inactive material in the sensing area to improve the performance [7, 2]. As many different aspects pay a role in the detector and sensor design, a prototype sensor called Monolithic Stitched Sensor (MOSS) has been developed and will be presented in the following section.

3.2 The MOSS and babyMOSS Prototypes

As part of the development of the ITS3 several prototype sensors have been developed, among them the MOSS. A detailed description and characterization of the sensor can be found here [17]. As already mentioned the MOSS is a stitched, wafer-scale and ultra thin MAPS prototype. It consists of ten Repeated Sensor Units (RSUs) produced on a single wafer and connected through stitching. The full sensor features readout and power distribution implemented in end-cap regions on either side of the stitched sensor. In principle, the left end-cap is sufficient to read out all ten RSUs, demonstrating the feasibility of large-area stitched MAPS devices. During characterization campaigns, alternative readout schemes are used to allow detailed performance studies of individual regions [2].

Due to the geometry of the silicon wafer, only six full-size sensors can be fabricated in a single production run. This leaves substantial areas of the wafer unused. To maximize the utilization of the available wafer surface, additional reticle-sized sensors are produced in these otherwise unused regions. These smaller devices are referred to as baby Monolithic Stitched Sensor (babyMOSS) sensors. A wafermap is shown in figure 3.2.

The babyMOSS sensors are geometrically and functionally identical to a single RSU of the full-scale MOSS detector but also have end-caps for readout and powering. The overall dimensions of a single RSU are $14\,\mathrm{mm} \times 25.9\,\mathrm{mm}$ and it consists of

eight pixel matrices, referred to as *regions*. Four regions, indexed from 0 to 3, are arranged side by side to form a Half Unit (HU). Two half-units are stacked vertically, resulting in a *top* and a *bottom* half-unit. All regions in the top HU contain an identical amount of pixels arranged in a 256×256 matrix, corresponding to a pixel pitch of $22.5\ \mu\mathrm{m}$. In contrast, the regions in the bottom HU consist of 320×320 pixels each, resulting in a smaller pixel pitch of $18\ \mu\mathrm{m}$. Each of the HUs is equipped with independent power and readout infrastructure, enabling individual configuration and characterization per region.

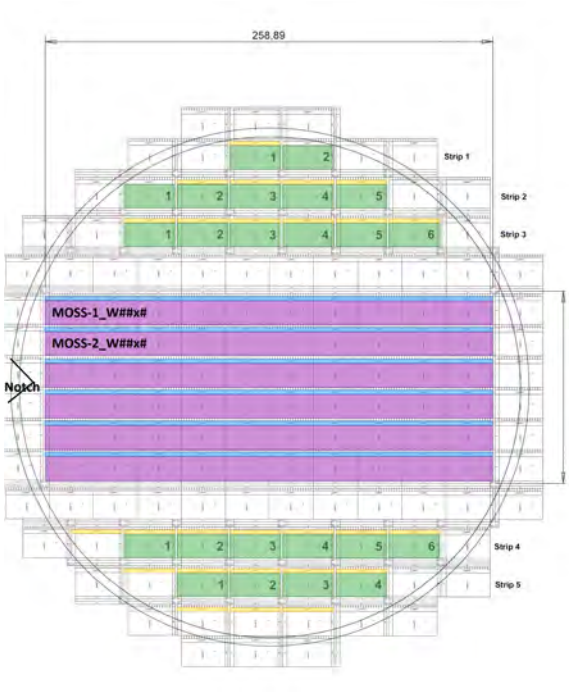


Figure 3.2: Schematic wafermap with six MOSS in the center and 23 babyMOSS in the remaining space on the wafer. Taken from [18]

As this is a prototype not all regions follow the same chip design regarding their front-end to test differences in performance. While no exact information on the design is given, it is known that only top region 0 and bottom regions 0 to 2 have the standard in-pixel front-end as shown in figure A.1. In the top HU region 1 has a larger input transistor (M1) to reduce noise, region 2 has a larger discriminator input transistor (M11) reducing threshold dispersion and region 3 has a larger common-source transistor (M2) to increase the gain. The bottom region 3 has a different layout with changes to the parasitic capacitance [17].

The sensor operation is controlled via several bias parameters, among which the discriminator threshold is mainly set by the voltage V_{casb}. Increasing V_{casb} lowers the effective threshold, enhancing hit detection at the cost of increased noise and fake-hit rate. Another key parameter is V_{psub}, which defines whether the sensor is operated in forward- or reverse-bias mode and thereby directly influences the charge collection properties and operating point of the front-end.

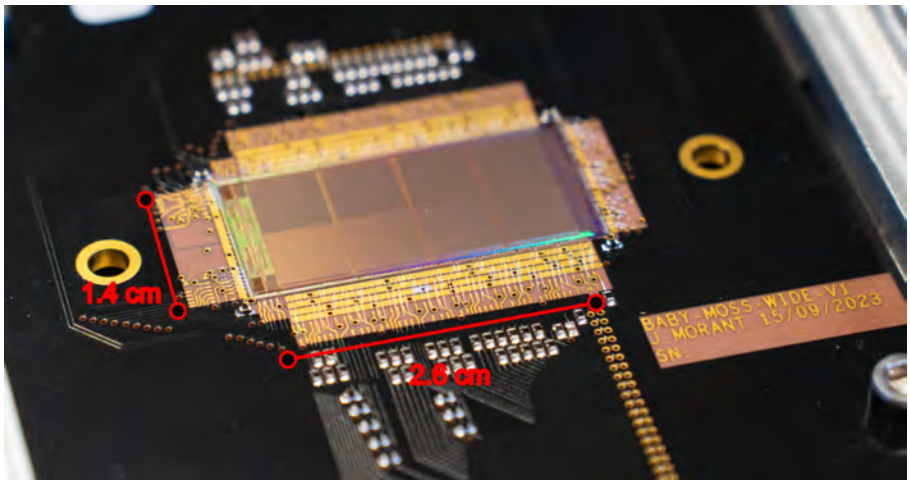


Figure 3.3: Photograph of a babyMOSS sensor mounted on its carrier Printed-Circuit Board (PCB). Photograph taken by L. Halstenberg; Annotations by A. Rachev.

In order to operate the babyMOSS it has to be connected to a carrier printed circuit board. This process requires precise operation. First, the silicon sensor is aligned to the PCB and then glued into place with the help of a robot. The sensor is then wire bonded to the PCB with a specialized bonding machine after curing. The whole process including power and impedance testing can be found here in detail [19]. A picture of the sensor on the carrier board is shown in figure 3.3. The entire test setup and data acquisition with the babyMOSS is further described in chapter 4.

Due to its modular structure, defined geometry and configurable operating parameters, the babyMOSS provides an platform for detailed sensor characterization. The results obtained with babyMOSS sensors form an essential input for the optimization of the final ITS3 sensor design [7, 2].

Experimental Methods – Beam Telescope

4

In order to analyze different properties of particle detectors, a beam telescope can be used. In this chapter, the general concept of a beam telescope and all components of the setup used for the measurements are presented.

As depicted in 4.1 a beam telescope consists of several tracking planes placed along the beam axis. In the center is the DUT while the planes in the front and behind serve as reference planes. The number of reference planes can vary. However six are commonly used, three are placed upstream and three downstream, where *upstream* denotes the region in front of the DUT and *downstream* the region behind it.

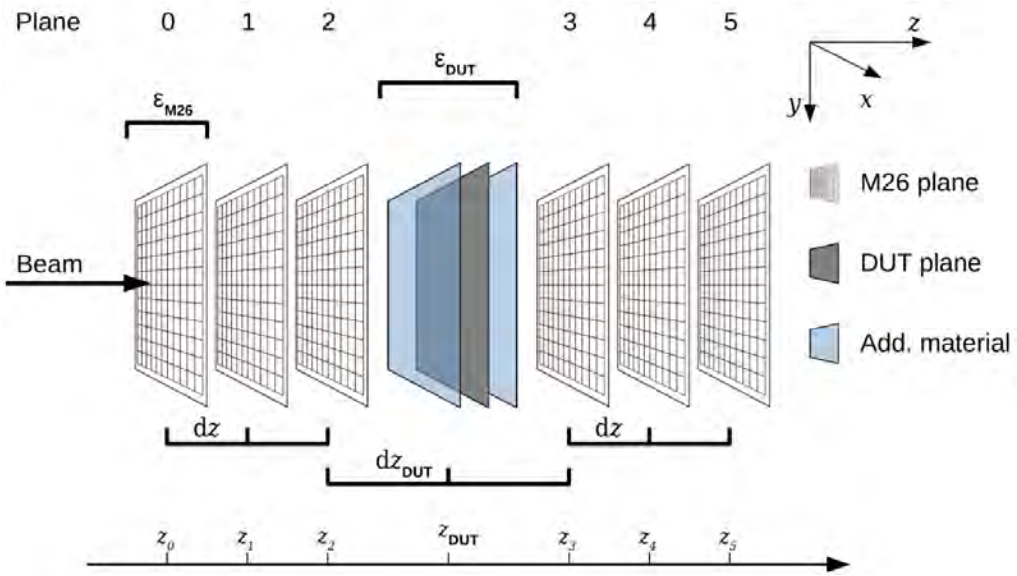


Figure 4.1: Schematic of a DESY-type telescope setup with six reference planes and one DUT. Taken from [8]

In order to trigger the readout, two scintillators are commonly used, one positioned upstream and one downstream of the setup, ensuring that a trigger signal

is generated only when a particle passes through both. This coincidence condition reduces noise and guarantees that only particles traversing the full setup are recorded. More details on this part of the setup are provided in 4.2.
When a charged particle passes through the telescope, it produces hits in each tracking plane. From the hits on the reference planes, a track is reconstructed, providing an accurate prediction of the particle's impact point at any position along the beam path. This reconstructed trajectory can then be used to analyze the properties of the DUT by comparing the predicted particle position at the DUT plane with the corresponding hit recorded by the DUT. The most important characteristics studied in this way are the detection efficiency, the fraction of correctly recorded hits, and the spatial resolution, which quantifies the positional accuracy of the detector.

4.1 Raiser-DAQ and Beam Telescope Setup

Each of the babyMOSS sensors is powered and operated through a combination of an Data Acquisition (DAQ) board, raiser board and carrier PCB as shown in figure 4.2. As mentioned in section 3.2 the detector itself is glued and wire bonded to the PCB which is connected to the DAQ board via raiser board. The raiser board serves as an interface between the two, while the powering and readout of the babyMOSS is managed through the DAQ board which is connected to a computer via USB. The interface is needed because the DAQ board was originally developed for the *ALPIDE* sensor, and requires different routing than the babyMOSS, hence it features a new front-circuitry. The sensor is controlled with the help of an Field-Programmable Gate Array (FPGA) located on the DAQ board. The FPGA has to be programmed with the appropriate firmware each time the system is powered on. This setup is sufficient for operational tests of the sensors and can now be built into different setups, like a beam telescope, for more specific testing. The beam telescope used for this thesis was developed and manufactured by Alexander Rachev [19]. An overview of the setup is shown in figure 4.3 and more detailed information on the telescope can be found in [19]. The mechanical housing as well as the base plate used to mount the sensors and the trigger system are made of aluminum. The overall dimensions of the telescope are $50\,\mathrm{cm} \times 50\,\mathrm{cm} \times 45\,\mathrm{cm}$. The supporting frame consists of modular aluminum profiles from *Rose+Krieger*, while the sides are closed with plain aluminum panels. Upstream and downstream openings are integrated into the housing to ensure an unobstructed passage of the beam. This



Figure 4.2: Photograph of the DAQ raiser Setup. From left to right: babyMOSS on carrier PCB, raiser board, DAQ board. Photograph by I. Panasenko.

design allows for parasitic operation with additional detectors placed behind the telescope and also enables operation with the beam entering from either side. Further cutouts are present in the housing panels to provide fixed feedthroughs for electrical connections, including banana sockets, *LEMO* connectors, and a USB-B to USB-A adapter.

The base plate features a regular grid of M6 threads with a spacing of $2.5\,\mathrm{cm}$. The pixel sensors are mounted on carrier PCBs, which are screwed onto custom-made aluminum holders. These holders can be positioned freely on the base plate in steps of $2.5\,\mathrm{cm}$ and fixed using M6 screws, allowing for a flexible adjustment of the sensor spacing along the beam axis. To reduce mechanical movement and prevent bending of the readout electronics, the DAQ boards of the reference planes are additionally connected to each other using spacers. Only the DUT, which is exchanged more frequently during operation, is not fixed at multiple points.

The telescope consists of six reference planes, arranged as two groups of three sensors upstream and downstream of the DUT position. The gap between these two groups, visible in figure 4.3, accommodates the DUT. All sensors, including the DUT, are operated using the same DAQ and raiser board architecture.

For triggering, two scintillator detectors are installed upstream and downstream of the sensor planes. Each scintillator consists of a plastic scintillator of type *Scionix EJ-200* with dimensions $35\,\mathrm{mm} \times 25\,\mathrm{mm} \times 5\,\mathrm{mm}$, coupled to a *Hamamatsu H10492-003* photosensor module with an integrated photomultiplier tube. The scintillators

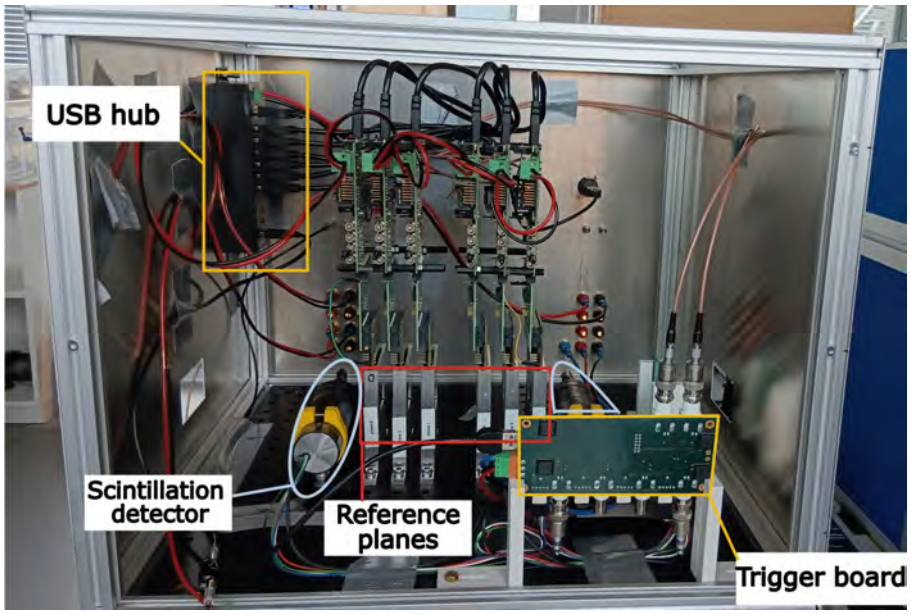


Figure 4.3: Photograph of the beam telescope setup (side view) used in the February 2025 test beam. The main components are colour-coded and labelled, including the reference planes, scintillators, USB hub, and trigger board. The DUT is not installed. Photograph by I. Panasenko; Annotations by A. Rachev.

are connected to a trigger board developed at CERN, which provides both the trigger logic and the regulation of the power supply for the trigger system. The trigger signals are routed using LEMO cables.

The trigger board is powered with $24\,\mathrm{V}$, supplied by a *Rohde&Schwarz HMP4040* laboratory power supply using two channels set to $+12\,\mathrm{V}$ and $-12\,\mathrm{V}$. The reference planes are powered by the same power supply via PCB connectors routed to banana sockets mounted on the telescope housing. To ensure stable operating conditions, all reference planes share a common supply channel, while the DUT is powered using a dedicated channel in order to prevent voltage fluctuations affecting the DUT measurements. For operating the DUT in back-bias mode, a dedicated LEMO cable connection is used. In addition, a USB hub is integrated into the setup to connect all readout and control systems to a single computer.

4.2 Trigger Chain

The scintillators upstream and downstream of the detector setup are connected to a trigger board, which in turn is connected to all detectors in a defined sequence,

as illustrated in figure 4.4. Whenever a particle produces a coincidence of signals in the Photomultiplier Tubes (PMTs), the trigger board generates a trigger signal. This signal is then propagated through all reference planes and finally reaches the DUT, where the detector issues a busy signal in response. The busy signal is sent back through all tracking planes to the trigger board.

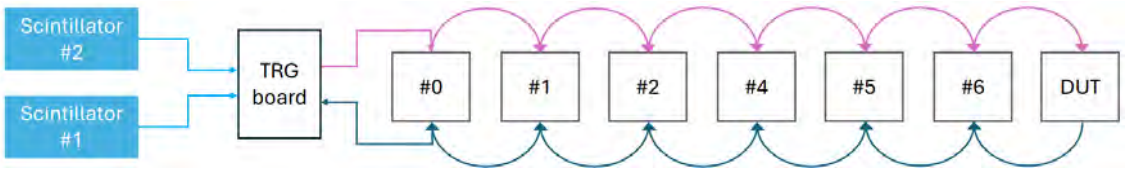


Figure 4.4: Schematic of the trigger chain of the babyMOSS telescope setup. Taken from [20].

The busy signal constitutes an essential part of the trigger–busy protocol: it prevents the system from issuing a new trigger while any detector is still processing data, ensuring that all planes contribute to a well defined and coherent event. If this timing coordination fails and a second trigger is accepted prematurely, detectors that are still occupied would have their readout interrupted, leading to a situation in which some planes record the event while others do not. Such inconsistencies compromise the event alignment across the telescope and can lead to desynchronization during the event building process.

4.3 Test Beam Facility (ELSA)

The measurements presented in this thesis were performed at the E3 beamline of the Electron Stretcher Facility (ELSA), a schematic overview of which is shown in figure 4.5. ELSA provides both polarized and unpolarized electron beams with energies of up to 3.2 GeV, which are generated in a three-stage acceleration process. In the first stage, a Linear Accelerator (LINAC) accelerates the electrons to an energy of 26 MeV before injecting them into a fast-cycling booster synchrotron. The booster further accelerates the electrons with a repetition rate of 50 Hz to a typical energy of 1.2 GeV, after which they are transferred to the stretcher ring [21].

The stretcher ring can be operated in three different modes, allowing the realization of a variety of experimental conditions within the same facility. Once the desired beam energy is reached, the beam can be extracted at two different locations. One extraction point serves the hadron physics experiments CBELSA [22] and

BGO-OD [23], while the second extraction point provides a dedicated beamline for detector tests, known as the E3 beamline [21].

The E3 beamline is designed to provide low-current electron beams, enabling particle rates in the range from approximately $1\,\mathrm{kHz}$ to $100\,\mathrm{kHz}$. In contrast, the high particle rates of up to several hundred megahertz used in hadron experiments would exceed the operational limits of pixel detectors under direct irradiation [21]. In order to archive higher particle rates in the E3 beamline, within some extend that is manageable for pixel detectors, the beamline can be supplied parasitically, while the beam is operated at conditions suitable for the hadron experiments. The extractions take place on their behalf, while part of the beam is extracted for the E3 beamline as well using a septum magnet. Thus the particle rate can not be controlled directly but depends on the position of the septum [24, 25].

While particle rates of several hundred kilohertz are, in principle, achievable at E3, the beam shows increasing fluctuations in position, size, and focus in between measurements where the beam rate is changed. In this work, the measurements were therefore limited to particle rates of up to $15\,\mathrm{kHz}$. It should be noted that there was no dedicated beam tuning by adjusting the quadrupole and dipole magnets during the data taking.

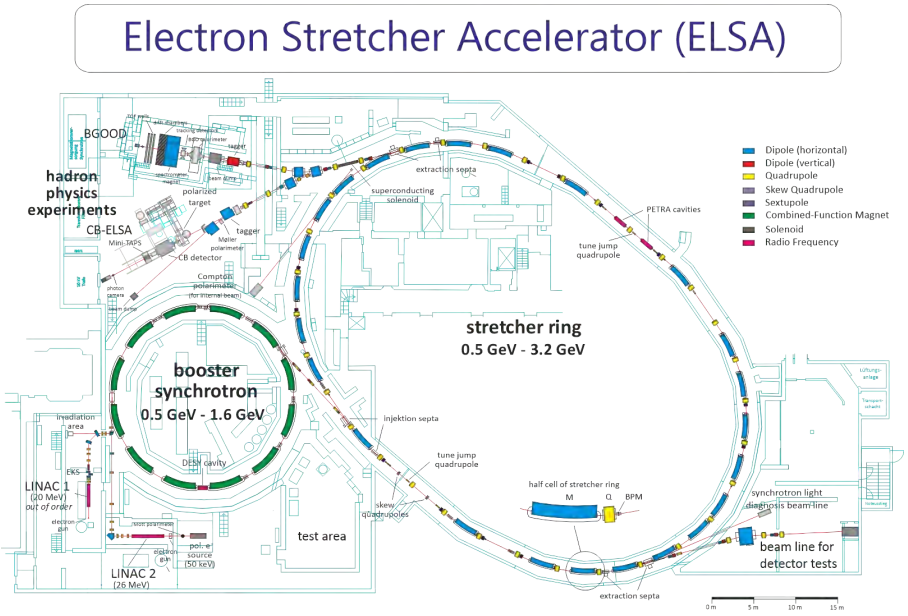


Figure 4.5: Schematic of the ELSA accelerator. Taken from [21].

4.4 Data Taking and Acquisition

After the telescope is fully assembled, all components including the trigger system, the power supplies, and the sensors are tested for functionality. For the sensor characterization, several Fake Hit Rate (FHR) and Threshold (THR) scans are performed. The FHR is measured by initiating triggers several thousand times and recording the amount of hits per pixel per unit time. For the THR scan increasing charges are injected and the state of the pixel is recorded several times per charge. The resulting distributions are shown in figure A.18 and figure A.19. The THR scans are carried out using the standard operating settings of the babyMOSS sensor at $V_{\text{casb}} = 15\,\text{DAC}$ and $V_{\text{psub}} = 0\,\text{V}$. They provide information on the region characteristics as well as the effect of the selected DAC settings on the overall pixel threshold. Besides this, deviating threshold values indicate malfunctions of single pixels or the matrix, which allows the scan to be utilized for diagnostics of the pixel matrices. Thus, the scans are used to identify noisy or defective pixels that can subsequently be masked. The threshold distributions confirm that the sensor operates within the expected range.

The FHR scan is used to determine the lowest possible discriminator threshold at $V_{\text{psub}} = -1.2\,\text{V}$ for which the sensor exhibits negligible fake-hit activity. For all regions, no fake hits are observed, except for bottom region 3, where four hits are registered. This corresponds to a fake-hit rate of $(3.3 \pm 0.6) \times 10^{-9}$ hits/pixel/event, which is well below the ITS3 requirement of 10^{-6} hits/pixel/event.

The data acquisition of the beam telescope is handled by the *EUDAQ 2* framework, which provides a modular and experiment-independent solution for synchronizing the readout of multiple detector systems [26]. A *EUDAQ* configuration file is used to define and address all components of the telescope, including the sensor planes, trigger scintillators, power supplies, and additional monitoring devices such as temperature sensors as *EUDAQ* producers. The data output of each producer is collected and written into a combined file in a raw binary format, which is then written to a disk.

Measurements are performed in runs. For each run the sensor settings can be varied, to test differences in the performance. In this work the *EUDAQ* configuration stays the same, while the varied parameter for the measurements is the beam rate, which is controlled seperately. Once a run is started, triggered events are recorded

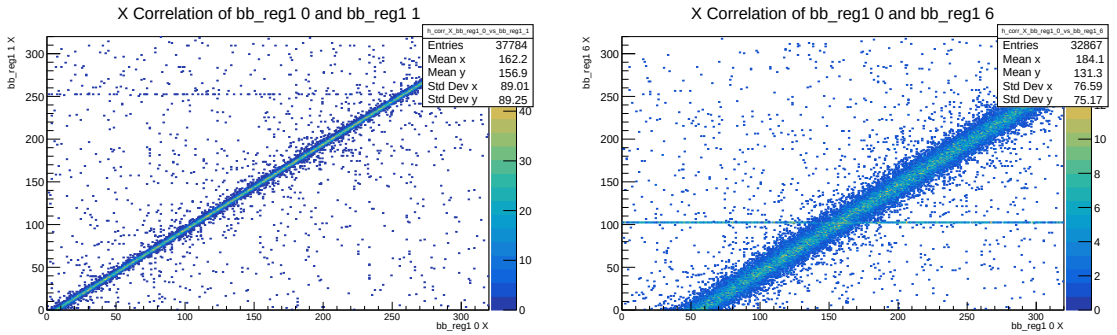


Figure 4.6: Photograph of the E3 beamline with two beam telescopes on the left and the and the beam pipe on the right. Surrounding the pipe are quadrupole magnet (yellow) and a dipole magnet (red). Photograph by L. Halstenberg.

and written in the *EUDAQ* raw data format. During test runs without beam, the trigger signal required for *EUDAQ* event building is generated by the trigger board, as no scintillator signals are available when running without a beam.

After completion of the initial tests, the telescope is installed in the beamline as shown in figure 4.6. The power supplies and the control computer are located underneath the telescope inside the beamline area. Since access to the beamline is not possible during beam operation, the system is controlled remotely via an Secure Shell (SSH) connection from an external computer.

A first coarse alignment of the telescope is performed using a laser to indicate the expected position of the beam center. An alignment is necessary, as effects such as charge sharing and multiple scattering, although reduced due to the low material budget compared to other setups, can still influence the measured results. Once the beam is switched on and the first test measurements are recorded, the alignment is verified using the data. For this purpose, the raw data are processed with the *EUDAQ* 2 *StandardEventMonitor*, which provides hitmaps for all sensor regions as well as correlation plots between regions in different detector planes. Examples of correlations between regions in plane 0 and plane 1, as well as between plane 0 and plane 6, are shown in figure 4.7. For an optimally aligned telescope, the



(a) (b)

Figure 4.7: Correlation of the hit positions along the x-axis for bb region 1, shown for the plane pairs (a) plane 0–plane 1 and (b) plane 0–plane 6.

correlations are expected to form a diagonal line passing through the origin with a slope of one, indicating a one-to-one correspondence between hit positions in the respective planes. The correlations shown correspond to the horizontal (x) direction. A small offset from the origin is observed in the correlation between plane 0 and plane 1, indicating a slight horizontal rotation of the telescope. This interpretation is supported by the correlation between plane 0 and plane 6, where a larger displacement in the x direction is visible, corresponding to a shift of a few millimeters in physical coordinates.

The deviations indicate a non-ideal alignment, further corrections can only be applied through manual mechanical adjustments of the telescope. Given that the observed offsets are already on the millimeter scale, additional manual corrections are not expected to lead to a significant improvement. The same procedure is then applied to the correlations in the vertical (y) direction, where deviations of comparable magnitude are observed. Consequently, the alignment is considered sufficiently accurate.

Measurements are performed at ten different beam rates: $500\,\mathrm{Hz}$, $1\,\mathrm{kHz}$, $2\,\mathrm{kHz}$, $3\,\mathrm{kHz}$, $4\,\mathrm{kHz}$, $5\,\mathrm{kHz}$, $6\,\mathrm{kHz}$, $8\,\mathrm{kHz}$, $10\,\mathrm{kHz}$, and $15\,\mathrm{kHz}$. For each beam rate, at least $100{,}000$ triggered events are recorded per sensor, distributed over all regions. The total number of recorded events is determined by the trigger rate provided by the scintillator detectors. The resulting raw data sets form the input for the subsequent offline reconstruction and analysis, which are described in the following section.

4.5 Data Analysis with Corryvreckan

The information presented in this chapter is primarily based on the *Corryvreckan User Manual* [27], further details on individual modules and the general software concept can be found therein. The *Corryvreckan* framework is a modular reconstruction and analysis software developed for test beam experiments with pixel detectors. The software provides an environment in which individual processing steps are implemented as independent modules that can be combined and configured through external configuration files. This modular structure allows the reconstruction chain to be adapted to different detector setups and analysis chains.

```
# BabyMOSS plane 2
[bb_reg0_2]
type = "MOSS"
position = 0mm,0mm,50mm
number_of_pixels = 320,320
pixel_pitch = 18um, 18um
spatial_resolution = 5.2um, 5.2um
time_resolution = 10s
material_budget = 0.0005
coordinates = "cartesian"
orientation = 0deg,0deg,0deg
orientation_mode = xyz
role = "reference"

# BabyMOSS plane 3
[bb_reg0_3]
type = "MOSS"
position = 0mm,0mm,75mm
number_of_pixels = 320,320
pixel_pitch = 18um, 18um
spatial_resolution = 5.2um, 5.2um
time_resolution = 10s
material_budget = 0.0005
coordinates = "cartesian"
orientation = 0deg,0deg,0deg
orientation_mode = xyz
role = "DUT"
roi = [[0,0], [0,220], [320,220], [320,0]]
```

Figure 4.8: Geometry file of one reference plane and the DUT plane.

For the analysis presented here, the experimental setup is identical for all measurements, consequently the same analysis workflow can be applied consistently to all data sets. A necessity for each step of the analysis is the definition of appropriate geometry files. As example a part of an geometry file is shown in figure 4.8.

Each detector region requires an individual geometry file, as the regions are spatially separated and do not form a contiguous detector area. Within a single geometry file, the properties of all seven planes of the beam telescope are defined. The coordinate system used in the geometry description is a right-handed Cartesian system originating from the lower left corner of the detector. The detector planes extend in the x–y plane, while the positive z direction follows the beam axis. For different detector planes, only the position along the z axis is varied. Additional parameters defined in the geometry files include the spatial resolution, assumed here to be the binary resolution, the pixel pitch, the number of pixels, the material budget, as well as the

detector type and its assigned role within the telescope. The latter is used to define which plane is used as the reference plane in the alignments and which is the DUT. Depending on the analysis module applied, the geometry files are modified internally by *Corryvreckan*, for example during the masking or alignment procedures, as discussed in section 4.5.1 and section 4.5.4. The individual steps of the track reconstruction and analysis workflow are described in the following sections.

4.5.1 Masking

The first step of the analysis consists of the identification and masking of noisy pixels. Pixels exhibiting excessive noise or an unusually high hit rate can distort the reconstruction process and bias performance observables, and therefore are excluded from further analysis by applying pixel masks. In *Corryvreckan*, masking is performed prior to the reconstruction of clusters and tracks to ensure that only reliable pixel information is used in the subsequent analysis steps. The masking procedure used in this analysis is based on the average pixel hit frequency within a given region: pixels whose hit frequency exceeds the mean pixel hit rate by a predefined frequency cut are classified as noisy. For the data analyzed in this work, a frequency cut of 200 is applied, meaning that pixels with a hit rate at least 200 times larger than the regional average are masked.

```
[Corryvreckan]
detectors_file         = "\path\file.conf"
detectors_file_updated = "\path\file.conf"
number_of_events = -1

[Metronome]
triggers=1

[EventLoaderEUDAQ2]
file_name = "\path\data.raw"

[MaskCreator]
frequency_cut=200
write_new_config=true
```

Figure 4.9: Configuration file for the masking.

In order to achieve the former, a dedicated configuration file in which the frequency cut, along with the paths to the raw input data and the corresponding detector file needs to be defined. After the masking procedure, a mask file is generated for each region and for each detector plane. The path to the resulting mask file is then added to the detector file, and the path and name of the updated detector description are specified in the configuration file. An example of the masking configuration is shown in figure 4.9.

4.5.2 Clustering

The clustering step is not performed only once, but is repeated after each stage of the analysis workflow that modifies the geometric description of the detector. This ensures that the cluster positions are updated according to the refined hit positions following alignment corrections. Clustering reduces the raw pixel information to a single hit position per particle and detector plane, which is required for track reconstruction. For detectors providing only binary hit information, the cluster position is determined from the arithmetic mean of the positions of neighbouring pixels belonging to the same cluster.

4.5.3 Prealignment

Before the alignment procedure is applied, a prealignment step is performed. In this step, the detector planes are aligned translationally along the x and y axes, while rotational misalignments are not yet considered. The DUT is excluded from the prealignment procedure in order to avoid introducing biases at a later stage in the performance analysis.

```
[Corryvreckan]
detectors_file         = "\path\file.conf"
detectors_file_updated = "\path\file.conf"
number_of_events = -1

[Metronome]
triggers=1

[EventLoaderEUDAQ2]
file_name = "\path\data.raw"

[ClusteringSpatial]
use_trigger_timestamp  = 0
charge_weighting       = 1
reject_by_roi          = 1

[Correlations]

[Prealignment]
method=gauss_fit
fit_range_rel=200
time_cut_abs=1e99
exclude_dut = true
```

Figure 4.10: Configuration file for the prealignment.

The translational alignment corrections are obtained from the correlations of hit positions in the x and y directions with respect to the defined reference plane (see figure 4.8). The shifts are determined from the mean of the corresponding one-dimensional correlation distributions which is, in this work, obtained from a Gaussian fit to the distributions. Thus there is no tracking required for the translational corrections. At this stage, centering the spatial correlations around zero provides an acceptable initial approximation for prealignment, although this must not be enforced in the final alignment where physical displacements of the planes have to be preserved.

For the prealignment procedure, a dedicated configuration file is required, an example of which is shown in figure 4.10. In addition to the file and detector parameters, this configuration includes the `Prealignment` module as well as the `Clustering` module, which is executed to ensure consistency between updated detector positions and reconstructed clusters.

4.5.4 Alignment

Following the prealignment, the detector geometry is refined by applying both translational and rotational alignment corrections. Two different alignment methods are used in this analysis, both of which require the reconstruction of particle tracks. Consequently, all alignment configuration files include the `Tracking4D` module. A part of an alignment configuration file is shown in figure 4.11, only new modules are inserted. For the alignment procedure, track reconstruction is performed using a straight-line fit, which provides an efficient and sufficiently accurate description of the particle trajectories at this stage. Alternatively, a General Broken Lines (GBL) fit can be employed, archiving comparable results. The tracking configuration requires a minimum of six hits per track, as the alignment is initially performed without including the DUT. Additional parameters specified for the tracking include the particle momentum and a spatial selection cut, which is iteratively reduced to $30\,\mu$m to improve the alignment precision.

```
[ClusteringSpatial]
use_trigger_timestamp  = 0
charge_weighting       = 1
reject_by_roi          = 1

[Tracking4D]
track_model="straightline"
min_hits_on_track=6
time_cut_abs=1e99
momentum=2.9GeV
exclude_dut = 1
spatial_cut_abs=1mm,1mm
unique_cluster_usage=true

[FilterEvents]
max_tracks             = 1

[AlignmentTrackChi2]
iterations             = 3
align_position         = 1
align_orientation      = 0
prune_tracks           = 0
max_associated_clusters = 1
max_track_chi2ndof     = 50
exclude_dut = true
```

Figure 4.11: Part of an alignment configuration file. Modules that were already shown in other configuration files are excluded from this graphic.

The alignment itself is performed using the `AlignmentMillepede` as well as the `AlignmentTrackChi2` modules. The

AlignmentMillepedemodule determines the optimal alignment parameters by simultaneously fitting track parameters and alignment constants. This procedure follows the Millepede algorithm [28]. The AlignmentTrackChi2 module evaluates the disagreement between measured hit positions and the positions predicted by the reconstructed tracks. The detector geometry is iteratively adjusted to minimize the resulting χ^2, thereby reducing the discrepancies between the track model and the detector positions.

Once the reference planes are properly aligned, the DUTAssociation and AlignmentDUTResidual modules are added to complete the alignment procedure including the DUT. During the association step, a spatial cut is applied to associate DUT clusters to reference tracks, while clusters exceeding this cut are excluded to suppress outliers. The subsequent residual-based alignment minimizes the residuals, defined as the distance between the reconstructed track position and the associated cluster on the DUT plane.

After the alignment procedure is completed, the final analysis is performed using the AnalysisDUT and AnalysisEfficiency modules. These modules extract the relevant performance observables and store the results in a *ROOT* file. The analysis results and their interpretation are presented in the following chapter.

5 Analysis

This chapter presents the analysis of the data recorded during the February 2025 test beam campaign at the ELSA facility in Bonn. The goal is to evaluate the performance of the DUT **babyMOSS-3_2_W05D5** in terms of detection efficiency and spatial resolution under different particle rates across several regions. This is the only sensor that has been tested in the scope of this thesis, thus all results are related to it.

Table 5.1: Information about the DUT that was used and the settings it ran with during all measurements.

babyMOSS-3_2_W05D5
non irradiated
Pitch top: $22.5\,\mu\mathrm{m}$
Pitch bottom: $18\,\mu\mathrm{m}$
$\mathrm{I_{bias}} = 62\,\mathrm{DAC}$
$\mathrm{I_{biasn}} = 100\,\mathrm{DAC}$
$\mathrm{I_{reset}} = 10\,\mathrm{DAC}$
$\mathrm{I_{db}} = 50\,\mathrm{DAC}$
$\mathrm{V_{shift}} = 145\,\mathrm{DAC}$
$\mathrm{V_{casn}} = 104\,\mathrm{DAC}$
$\mathrm{V_{psub}} = -1.2\,\mathrm{V}$
$\mathrm{Strobelength} = 6\,\mu s$
$\mathrm{T} = 27\,^{\circ}\mathrm{C} - 28\,^{\circ}\mathrm{C}$

The first part of the analysis focuses on the quality of the raw data and assesses its suitability for the subsequent analysis. After that the analysis results of the detection efficiency and the analysis of the spatial resolution are presented and discussed.

The measurements presented in this chapter were performed at the ELSA test beam with a particle energy of $2.9\,\mathrm{GeV}$ and beam rates ranging from $500\,\mathrm{Hz}$ up to $15\,\mathrm{kHz}$. All data were taken using identical sensor settings for the DUT as well as for the reference planes, all settings of the DUT besides the V_{casb}-value are summarized in table 5.1. The reference planes were operated at $V_{\mathrm{psub}} = 0$ and the V_{casb}-values are presented in the appendix listing A.1 they are the same for all reference plane. The discriminator threshold is primarily adjusted via the $\mathrm{V_{casb}}$ parameter and was chosen such that fake-hit contributions in the DUT are negligible. While the threshold scans

described in Section 4.4 were performed at lower V_{casb} values for sensor characterization, all measurements presented in this chapter were taken at a higher operating threshold to suppress fake hits. The selected V_{casb} value for the DUT was identical at $V_{casb} = 75\,\mathrm{DAC}$ units for all regions except for tb region 2 ($80\,\mathrm{DAC}$ units) and bb region 3 ($70\,\mathrm{DAC}$ units).

5.1 Raw Hitmaps and Beam Position

The hitmaps of all measurements show that the beam spot is not confined to a single region and that its position changes with the beam rate. Figures 5.1, and 5.2, and 5.4 show the hitmaps of the full sensor, containing both the top and bottom half-units, for increasing beam rates. At all beam rates, the hit density is non-uniform and predominantly concentrated in the bottom half-unit.

At a beam rate of $500\,\mathrm{Hz}$, about $75.32\,\%$ of all hits are recorded in bottom regions 0 and 1, forming a narrow horizontal band in the vertical direction. With increasing beam rate, the beam spot shifts towards higher region indices: at $1000\,\mathrm{Hz}$ the amount of hits in bottomregions 1 and 2 increases to $87.83\,\%$, while the vertical extent of the distribution remains largely unchanged.

At intermediate beam rates, the horizontal displacement is accompanied by a visible broadening of the hit distribution. For example, at $3000\,\mathrm{Hz}$ approximately $64.27\,\%$ of all hits are registered in bottom regions 2 and 3, indicating a reduced concentration compared to lower rates. This trend continues at $4000\,\mathrm{Hz}$, where the corresponding fraction decreases further to $53.58\,\%$, consistent with the increasingly diffuse hit pattern observed in the hitmaps. At $5000\,\mathrm{Hz}$ the beam spot shifts about one region to the left but is at $6000\,\mathrm{Hz}$ again illuminating region 3.

For high beam rates, the hit distribution extends over a large fraction of the sensor area. At $15\,\mathrm{kHz}$, a partial re-concentration of beam is observed, with $44.41\,\%$ of all hits located in bottom regions 2 and 3, although the overall distribution remains broader than at low beam rates.

The rate-dependent variations in the spatial hit distribution observed in the hitmaps already suggest potential complications for the further analysis, as changes in beam position and concentration affect the statistical weight of individual regions. Depending on the gratitude of the statistical deviations, a comparison of single regions can be taken into consideration rather than the sensor as one unit.

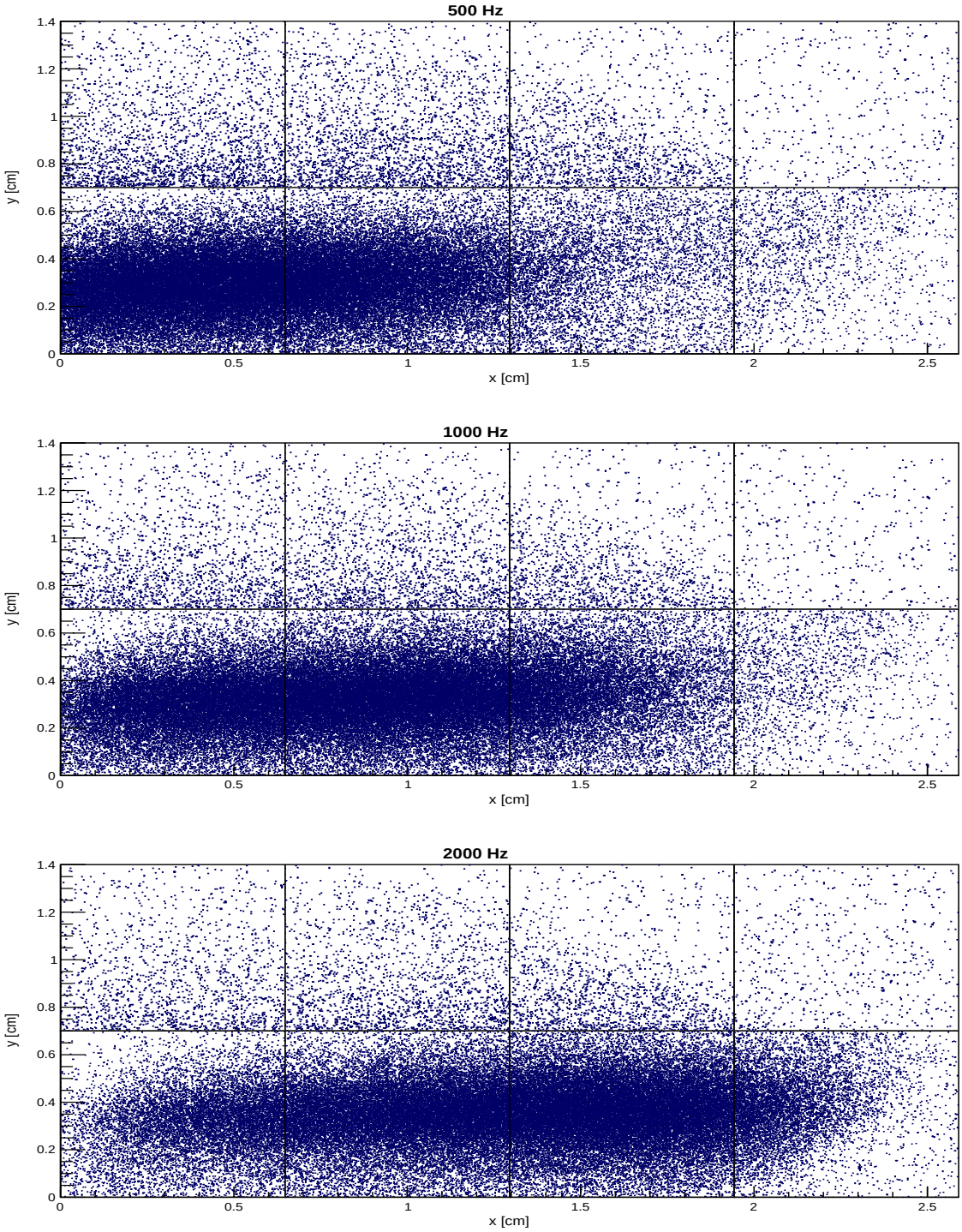


Figure 5.1: Hitmaps of the measurements with an approximated beam rate of $500\,\mathrm{Hz} - 2000\,\mathrm{Hz}$. Due to the different pixel pitch in top and bottom units the scale is altered resulting in an offset between top and bottom hitmaps.

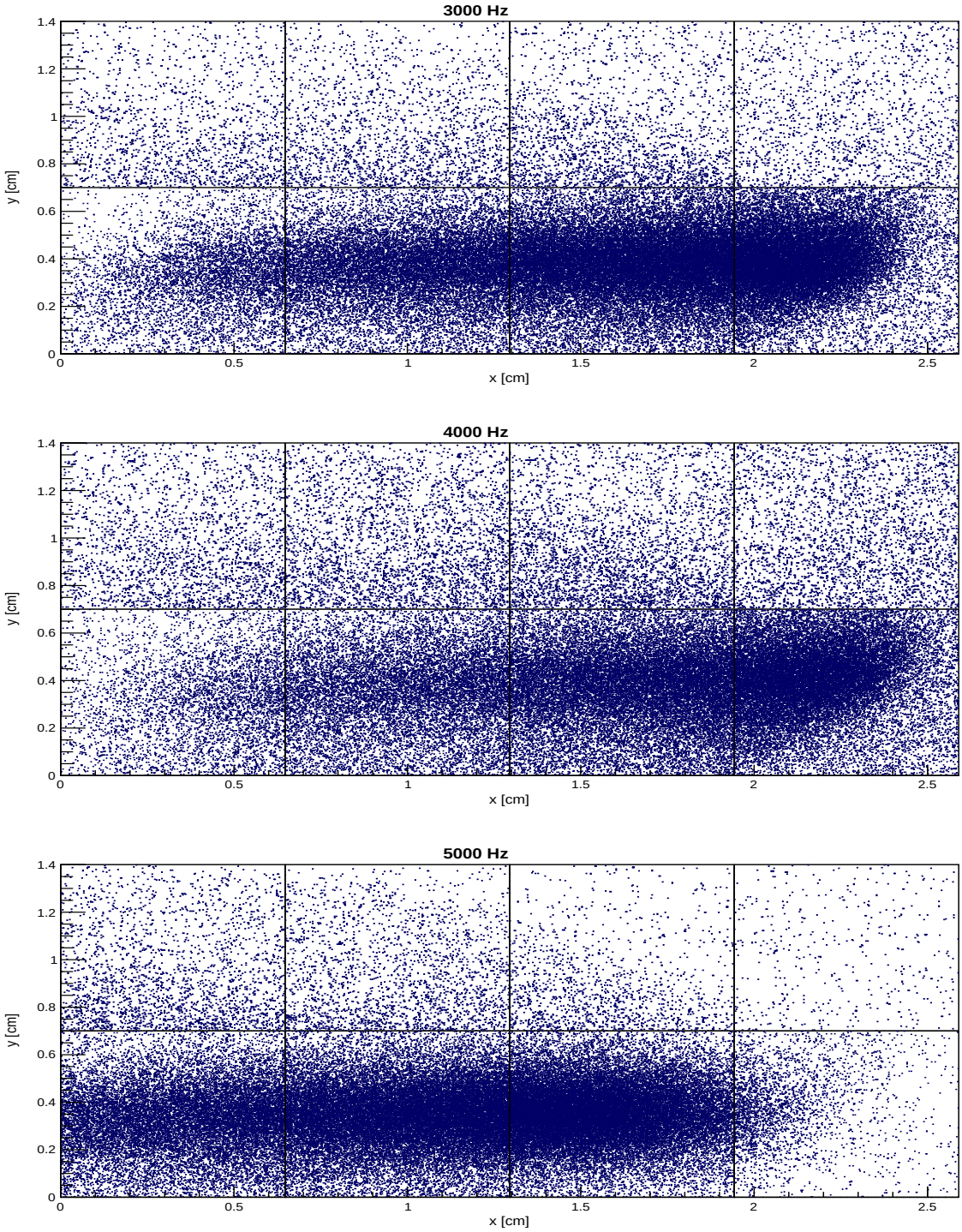


Figure 5.2: Hitmaps of the measurements with an approximated beam rate of $3000\,\mathrm{Hz} - 5000\,\mathrm{Hz}$. Due to the different pixel pitch in top and bottom units the scale is altered resulting in an offset between top and bottom hitmaps.

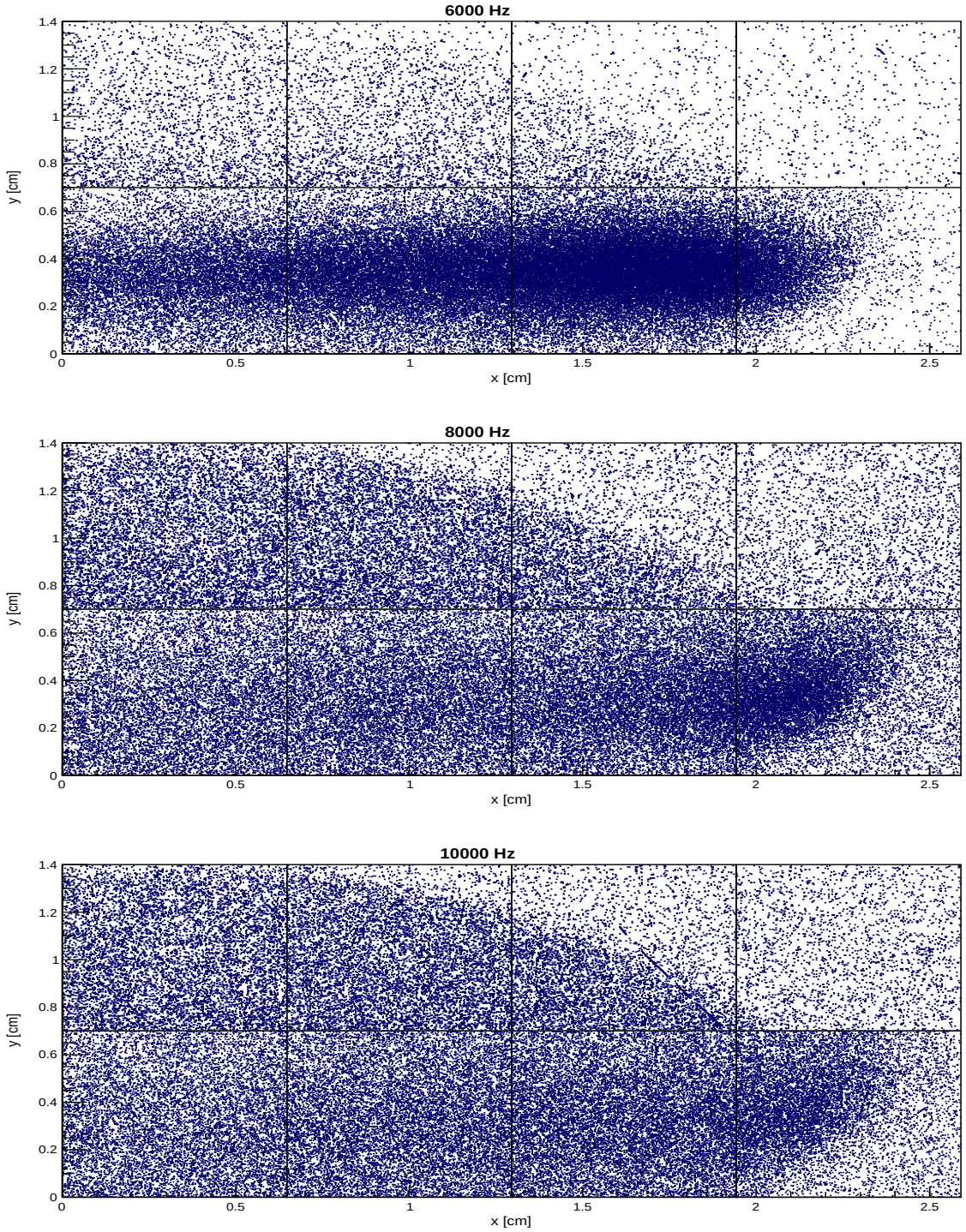


Figure 5.3: Hitmaps of the measurements with an approximated beam rate of $6000\,\mathrm{Hz} - 10000\,\mathrm{Hz}$. Due to the different pixel pitch in top and bottom units the scale is altered resulting in an offset between top and bottom hitmaps.

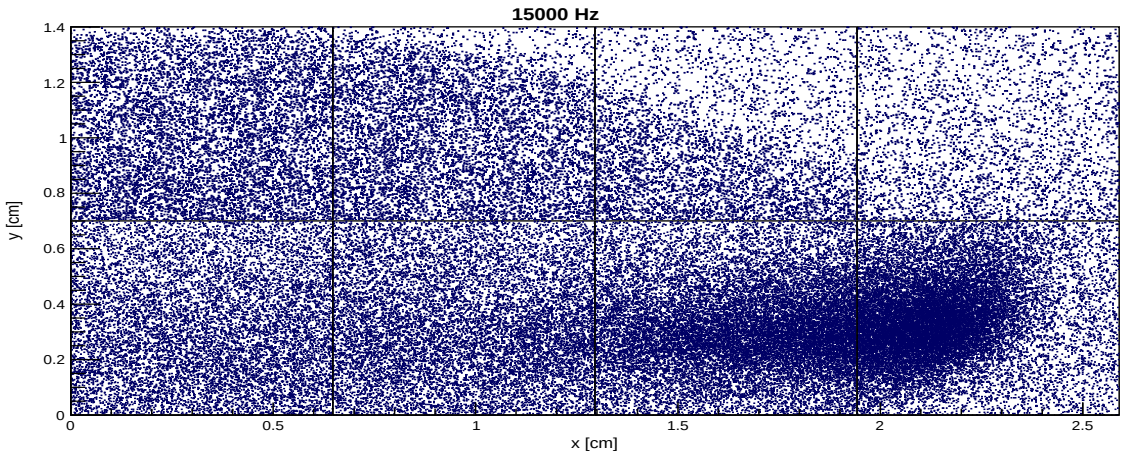


Figure 5.4: Hitmap of the measurement with an approximated beam rate of $15000\,\mathrm{Hz}$. Due to the different pixel pitch in top and bottom units the scale is altered resulting in an offset between top and bottom hitmaps.

Measurements at higher beam rates, originally planned up to $500\,\mathrm{Hz}$, had to be terminated at approximately $15\,\mathrm{kHz}$ due to limited beam stability. A possible reason for the inconsistencies in the beam size and concentration could be the operation mode. Running parasitically comes with the consequence that the beam rate can only be controlled by the positioning of the septum which could have an effect on the properties of the beam. This can not be proven by the available data and needs further research at ELSA for confirmation.

5.2 Detection Efficiency

The detection efficiency ε of the babyMOSS sensor was determined for each region using the *Corryvreckan* analysis framework and subsequently plotted as a function of the beam rate. For a direct comparison of top and bottom HUs, a plot of one representative region each is shown in figure 5.5 and figure 5.6. These regions were chosen as illustrative examples. The complete set of plots can be found in the Appendix appendix A.1.

The uncertainties are defined through the following. The total amount of tracks N_{trk} and the amount of tracks with associated cluster on the DUT N_{assoc} are obtained from the *Corryvreckan* framework. Each reconstructed track constitutes a binary trial, such that the statistical uncertainty of the efficiency follows binomial statistics. For measurements with limited statistics or efficiencies close to unity, asymmetric confidence intervals are used. In this case, the lower and upper bounds

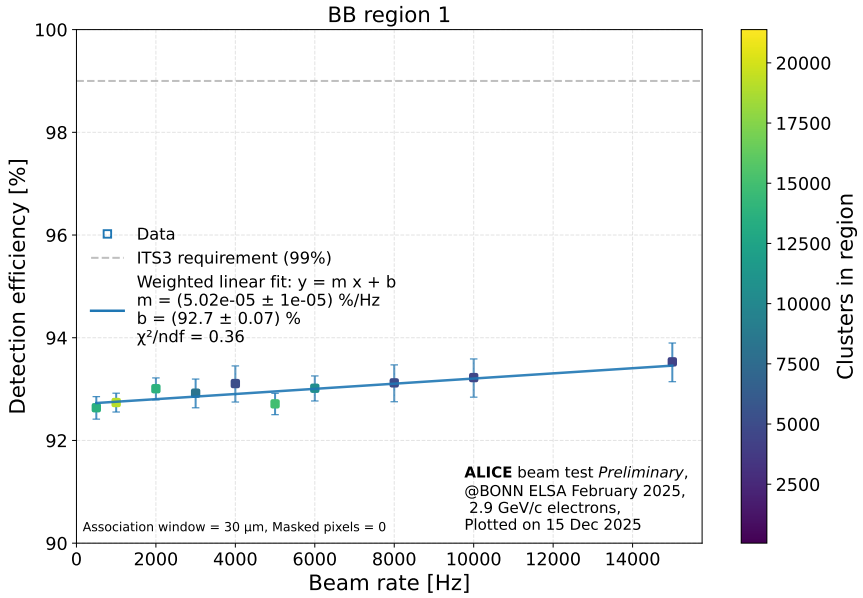


Figure 5.5: Detection efficiency of bottom region 1 in dependence of the beam rate. The data was fitted with a linear function.

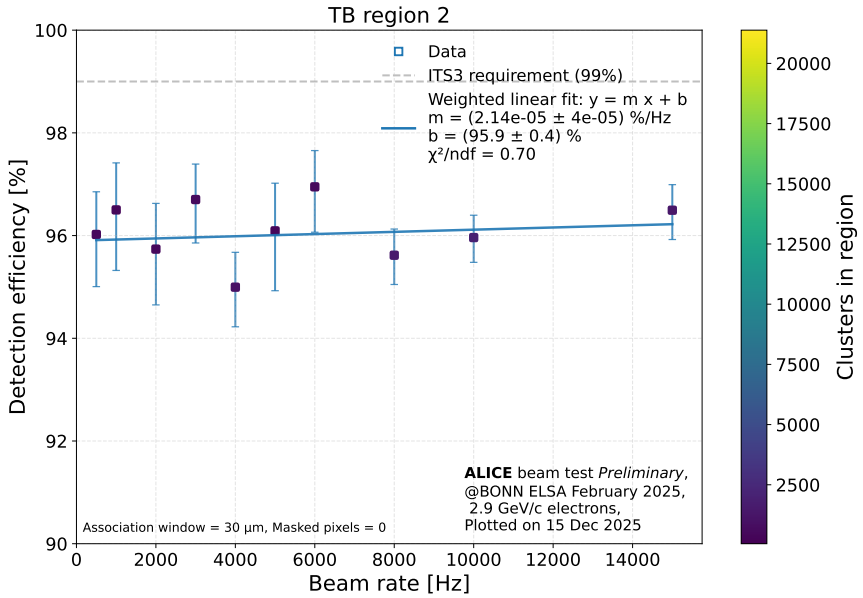


Figure 5.6: Detection efficiency of top region 2 in dependence of the beam rate. The data was fitted with a linear function.

of the efficiency are determined using the *Clopper–Pearson* method, resulting in asymmetric uncertainties:

$$\delta\varepsilon^{-} = \varepsilon - \varepsilon_{\text{low}}, \qquad \delta\varepsilon^{+} = \varepsilon_{\text{up}} - \varepsilon\,. \tag{5.1}$$

In practice, these confidence intervals are computed using the `TEfficiency` [29] class of the *ROOT* data analysis framework, which is employed by *Corryvreckan* for the calculation and visualization of efficiency observables. The asymmetric uncertainties obtained in this way are used for all efficiency values in this work.

Across the full range of beam rates studied, there is no significant change of the detection efficiency with increasing beam rate observable. Within each region in the bottom half unit, the observed point-to-point variations are consistent with statistical fluctuations and do not indicate a systematic dependence on the beam rate. Regions that were not directly illuminated by the beam show larger variations and increased uncertainties, which can be attributed to the lower number of reconstructed tracks and clusters. The color coding used in the plots indicates the number of associated clusters per region and highlights measurements with limited statistics.

To support the qualitative observation of the absence of a rate dependence, a linear function was fitted to the data in some regions. The extracted slopes are of the order of 10^{-5}, corresponding to an efficiency change of about $0.1\,\%$ for a beam rate increase of $10\,\text{kHz}$. Such variations are well within the statistical uncertainties of the measurements and are therefore not significant. The linear fits are not intended for extrapolation but are used solely to quantify the order of magnitude of possible rate-dependent effects within the investigated range. The detection efficiencies in top region 0 and top region 3 show large deviations of up to $3.5\,\%$ between two measurements, which could be caused by the low statistics available in these regions. Thus the data in these plots is not fitted with a linear function.

Independent of the beam rate, region-dependent differences in the average detection efficiency are observed. The average efficiencies per region, obtained by averaging over all beam rates, are summarized in Table 5.2. In the bottom half-unit, regions 0 and 1 show lower average efficiencies than region 2, although the regions are expected to operate uniformly as they are identical in construction. Bottom region 3 exhibits a higher average efficiency than the other regions, which is

consistent with expectations based on its modified capacitance and increased sensitivity to noise.

Table 5.2: Average detection efficiency per region, averaged over all beam rates.

HU	Region	Average efficiency (%)
bb	0	$92.94^{+0.36}_{-0.38}$
bb	1	$93.00^{+0.28}_{-0.29}$
bb	2	$94.90^{+0.24}_{-0.25}$
bb	3	$97.24^{+0.37}_{-0.46}$
tb	0	$94.67^{+0.73}_{-0.84}$
tb	1	$94.78^{+0.68}_{-0.77}$
tb	2	$96.11^{+0.71}_{-0.86}$
tb	3	$95.79^{+1.60}_{-2.49}$

The efficiencies measured in the top half-unit are, on average, higher than those of the bottom half-unit. However, the statistical uncertainties in the top regions are considerably larger, reaching values of up to $2.49\,\%$ for the averaged efficiency. For single measurements uncertainties of up to $4.88\,\%$ are reached. As a result, the apparent differences between the two half-units as well as between the top half regions are largely driven by limited statistics, and no quantitative conclusion on intrinsic performance differences between regions and half-units can be drawn from the present data.

It should be noted that the measured detection efficiencies remain below the ITS3 requirement of $99\,\%$. This behavior is expected and primarily related to the choice of the operating threshold, which was set conservatively in order to suppress fake hits. While this approach ensures a low fake hit rate, it inevitably leads to a reduction in detection efficiency. Independent measurements with varying threshold settings show detection efficiencies below $95\,\%$ at a V_{casb} value of 75 DAC, further illustrating the strong dependence of the efficiency on the chosen threshold configuration [19].

5.3 Spatial Resolution

As explained in section 2.4.3, the spatial resolution of a detector can be determined by analyzing the width of the residual distributions of each plane. The information

about the residuals is provided in the *ROOT* output files of the *Corryvreckan* analysis. The residual distributions are given separately for the global x and y coordinates. The width of the residual distribution is quantified by the standard deviation σ obtained from a Gaussian fit to the residual histogram. The quality of the residual distribution is strongly dependent on the available statistics. Distributions in regions with only a small number of hits tend to deviate from a Gaussian shape and are therefore affected by larger uncertainties. A comparison of fitted residual distributions with high and low statistics is shown in figure 5.7.

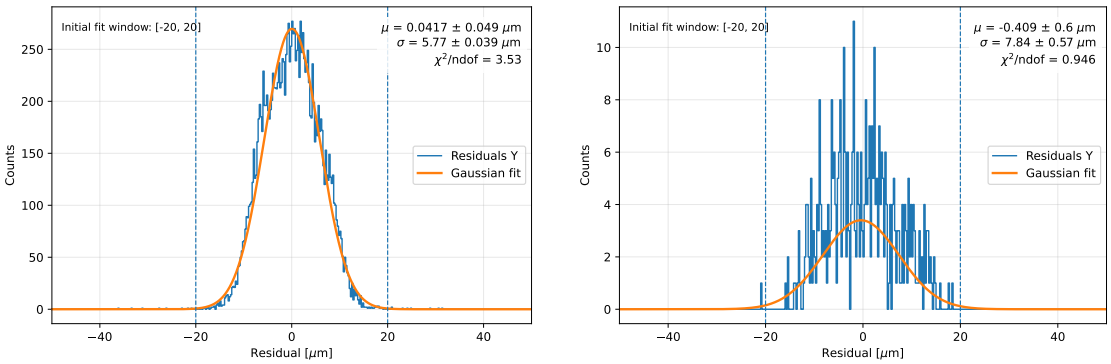


Figure 5.7: Residual distributions in the y direction for regions with high (left) and low (right) statistics.

The connection between the intrinsic resolution of the DUT, the track resolution, and the standard deviation of the Gaussian fit of the residuals is given by equation (2.7). The intrinsic spatial resolution of the DUT is obtained by subtracting the tracking contribution in quadrature:

$$\sigma_{\mathrm{DUT}}^{x,y} = \sqrt{\sigma_{\mathrm{res}}^{x,y\,2} - \sigma_{\mathrm{trk}}^{2}}\,, \tag{5.2}$$

where $\sigma_{\mathrm{res}}^{x,y}$ denotes the width of the fitted residual distribution in the x or y direction and σ_{trk} the track resolution at the position of the DUT.

The statistical uncertainty of the intrinsic spatial resolution is calculated using Gaussian error propagation [30],

$$\delta\sigma_{\mathrm{DUT}}^{x,y} = \frac{1}{\sigma_{\mathrm{DUT}}^{x,y}} \sqrt{\left(\sigma_{\mathrm{res}}^{x,y}\,\delta\sigma_{\mathrm{res}}^{x,y}\right)^2 + \left(\sigma_{\mathrm{trk}}\,\delta\sigma_{\mathrm{trk}}\right)^2}\,. \tag{5.3}$$

In the present analysis, the uncertainty of the track resolution is small compared to the statistical uncertainty of the fitted residual widths and is therefore neglected.

To obtain a single representative value for the spatial resolution in the sensor plane, the intrinsic resolutions in the x and y directions are averaged:

$$\sigma_{\mathrm{DUT}} = \frac{\sigma^x_{\mathrm{DUT}} + \sigma^y_{\mathrm{DUT}}}{2} \,. \tag{5.4}$$

Assuming uncorrelated uncertainties in the two directions, the uncertainty of the averaged spatial resolution is given by

$$\delta\sigma_{\mathrm{DUT}} = \frac{1}{2}\sqrt{\left(\delta\sigma^x_{\mathrm{DUT}}\right)^2 + \left(\delta\sigma^y_{\mathrm{DUT}}\right)^2} \,. \tag{5.5}$$

The intrinsic resolutions are determined separately in the x and y directions before averaging, as the quadratic subtraction of the track resolution represents a non-linear operation.

To estimate the track resolution, the *Telescope Optimizer* [31] tool is used. The required input parameters are summarized in Table 5.3. The geometrical configuration of the setup, referred to as the detector spacing, is taken from the setup described in Chapter 4.1. As an initial approximation for the resolution of the reference planes, the binary resolution is calculated using equation (2.5). The corresponding pixel pitches of the top and bottom half-units are $p_{\mathrm{tb}} = 22.5\,\mu\mathrm{m}$ and $p_{\mathrm{bb}} = 18\,\mu\mathrm{m}$, respectively.

Table 5.3: Input parameters used for the Telescope Optimizer.

Parameter	**Value**
Material budget x/X_0	$0.05\,\%$
Particle type	Electron (e^-)
Beam energy	$2.9\,\mathrm{GeV}$
Plane spacing	$2.5\,\mathrm{cm}$
Binary resolution (bb reference)	$5.2\,\mu\mathrm{m}$
Binary resolution (tb reference)	$6.5\,\mu\mathrm{m}$

For further improvement of the accuracy of the spatial resolution, the initially assumed binary resolution of the reference planes can be replaced by the calculated intrinsic resolution, iterating until convergence is reached. The convergence

is specified by the accuracy of the *Telescope Optimizer* which only allows inputs with up to two decimals. This step is skipped in the analysis, as the initially calculated spatial resolutions are close to the binary resolution. Thereby resulting in a minimal change in the spatial resolution of less than $0.1\,\mu\mathrm{m}$ for regions with the biggest deviation to the binary resolution.

For a direct comparison of top and bottom HUs, a plot of one representative region each is shown in figure 5.8 and figure 5.9. These regions were chosen as illustrative examples and are representative of the behavior observed across all regions that follow a certain trend. The complete set of plots can be found in the Appendix A.2.

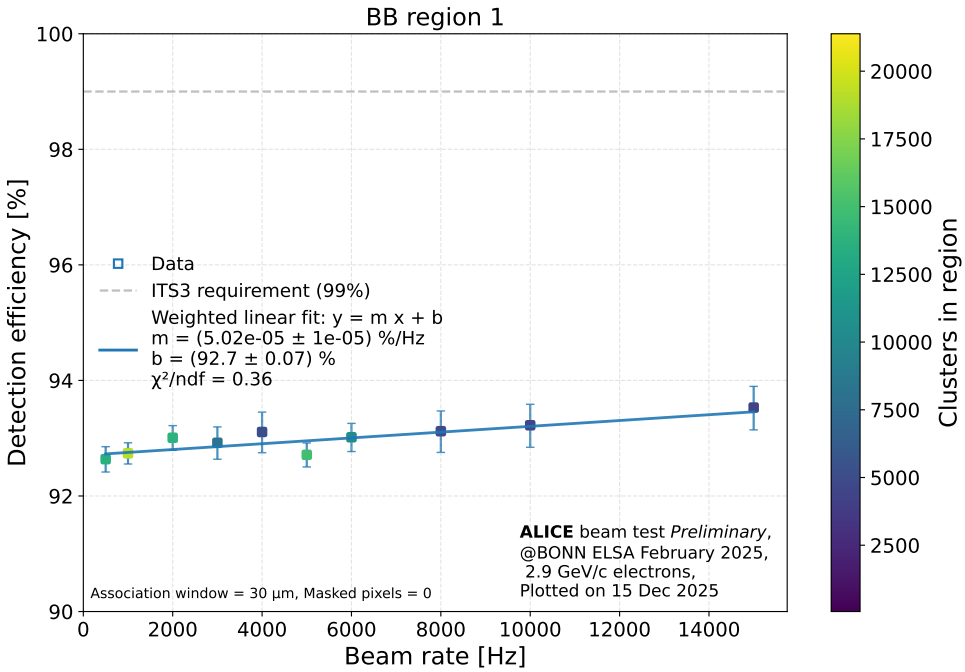


Figure 5.8: Spatial resolution of bottom region 1 as a function of the beam rate for a representative bottom half-unit region. The data was fitted with a linear function.

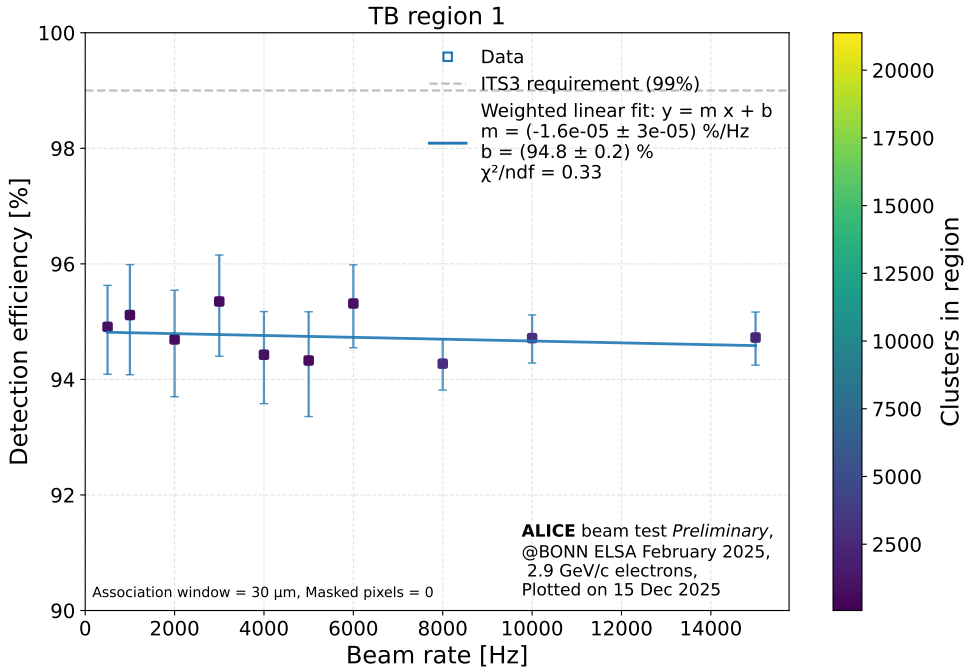


Figure 5.9: Spatial resolution of top region 1 as a function of the beam rate for a representative bottom half-unit region. The data was fitted with a linear function.

The data of all bottom regions and top region 1 is fitted with a linear function. The fitted slopes are of order $10^{-6}\,\mu\mathrm{m/Hz}$, corresponding to a variation of about $0.01\,\mu\mathrm{m}$ per $10\,\mathrm{kHz}$ increase in beam rate, indicating no significant rate dependence of the spatial resolution within the investigated range. No linear function was fitted to the data of region 0 and 2 of the top half-unit, as the reduced number of associated clusters and tracks induced statistical fluctuations showing no linear correlation between the spatial resolution and the beam rate. Additionally the spatial resolution in top region 2 at $4000\,\mathrm{Hz}$ exceeds the binary resolution limit. In top region 3, half of the data points exceed the limit, and three further points lie above the limit within uncertainties.

The average spatial resolution of the bottom half-unit is $(4.946 \pm 0.014)\,\mu\mathrm{m}$ and thus compatible with its binary resolution of $5.2\,\mu\mathrm{m}$. The average spatial resolution of the top half-unit also remains underneath its binary resolution of $6.5\,\mu\mathrm{m}$ with $(6.32 \pm 0.09)\,\mu\mathrm{m}$. Without considering the calculated resolution in top region 3 the value drops to $(6.16 \pm 0.03)\,\mu\mathrm{m}$. This behavior is consistent with the observed cluster sizes, which remains close to one for all regions, as summarized

in table A.1. The relatively high threshold setting suppresses fake hits efficiently but limits charge sharing between neighbouring pixels, resulting in position reconstruction that is largely dominated by binary information.

As a consequence, the achievable spatial resolution is close to the binary limit, in particular for the top half-unit. Additionally, the larger uncertainties observed for the top half-unit originate primarily from lower statistics, leading to less well-populated residual distributions and reduced stability of the Gaussian fits. Overall, the measured spatial resolution is limited by the chosen and given operating conditions. Measurements at lower thresholds and with higher statistics would be required to enhance charge sharing and to achieve a spatial resolution significantly below the binary limit.

5.4 Track Quality and Selection

The quality of the reconstructed tracks is monitored using the χ^2/ndof value of the track fits, as obtained from the track fitting performed within the Corryvreckan framework. Figure 5.10 shows the χ^2/ndof for the bottom region 0 at $500\,\mathrm{Hz}$.

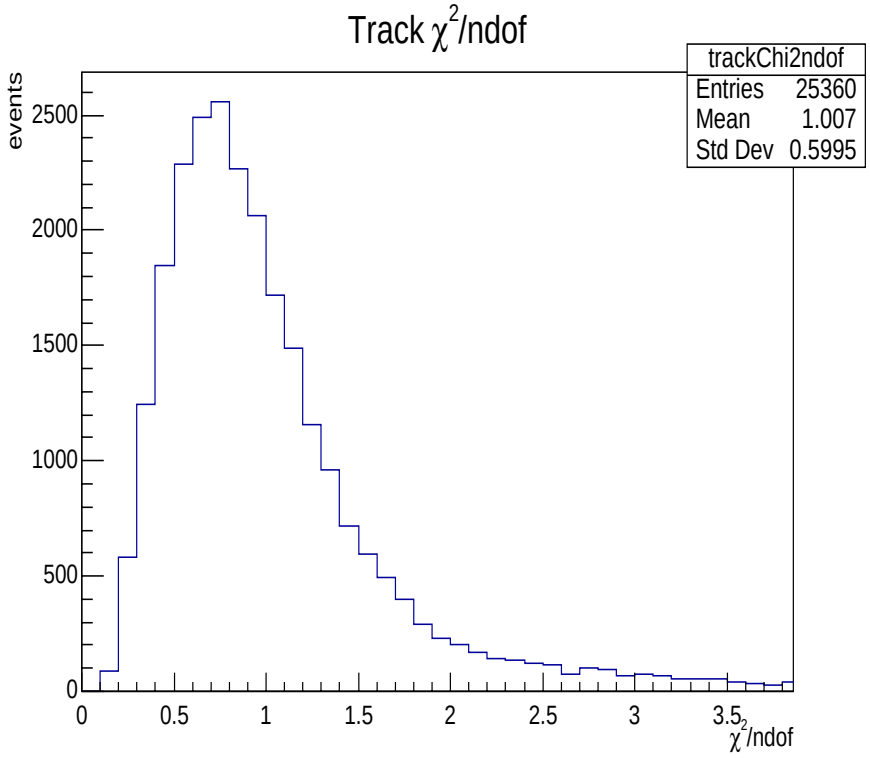


Figure 5.10: Reduced χ^2 of the fits for the tracks in bottom region 0 at $500\,\mathrm{Hz}$.

Tracks with $\chi^2/\mathrm{ndof} > 3$ are excluded from the analysis to suppress poorly reconstructed tracks. Such tracks would otherwise broaden the residual distributions and bias the extracted spatial resolution. The applied cut efficiently removes outliers while preserving the well-reconstructed tracks. The same track-quality selection is applied consistently in the determination of both the detection efficiency and the spatial resolution.

6 Summary and Outlook

The performance of a non-irradiated babyMOSS sensor was studied using test beam data recorded in February 2025 at the ELSA facility in Bonn with $2.9\,\mathrm{GeV}$ electrons. Detection efficiency and spatial resolution were evaluated for all sensor regions at beam rates between $500\,\mathrm{Hz}$ and $15\,\mathrm{kHz}$.

The raw hitmaps show a clear rate-dependent variation of the beam position and width, leading to an inhomogeneous illumination of the sensor. These effects limit the statistical comparability between regions and constrained the maximum usable beam rate to about $15\,\mathrm{kHz}$. This limitation is attributed to beam stability rather than to sensor or readout performance.

Within statistical uncertainties, no dependence of the detection efficiency on the beam rate is observed for any region. Region-dependent differences in the average efficiency are measured and are consistent with known variations in capacitance and noise sensitivity. The overall efficiencies remain below the ITS3 target value due to the intentionally high threshold setting used to suppress fake hits.

The spatial resolution shows no significant rate dependence and is found to be close to the binary limit, particularly for the bottom half-unit. This behavior is consistent with cluster sizes close to one, indicating limited charge sharing at the chosen operating point. The larger uncertainties observed in the top half-unit are mainly caused by reduced statistics.

Future measurements with improved beam stability and more homogeneous illumination would allow studies at higher particle rates and enable a more balanced comparison between regions. Measurements at lower thresholds are required to enhance charge sharing and to achieve spatial resolutions below the binary limit. In addition, extending the analysis to irradiated sensors is essential to assess the long-term performance of the MOSS technology for the ALICE ITS3 upgrade.

Additional Figures and Tables

A

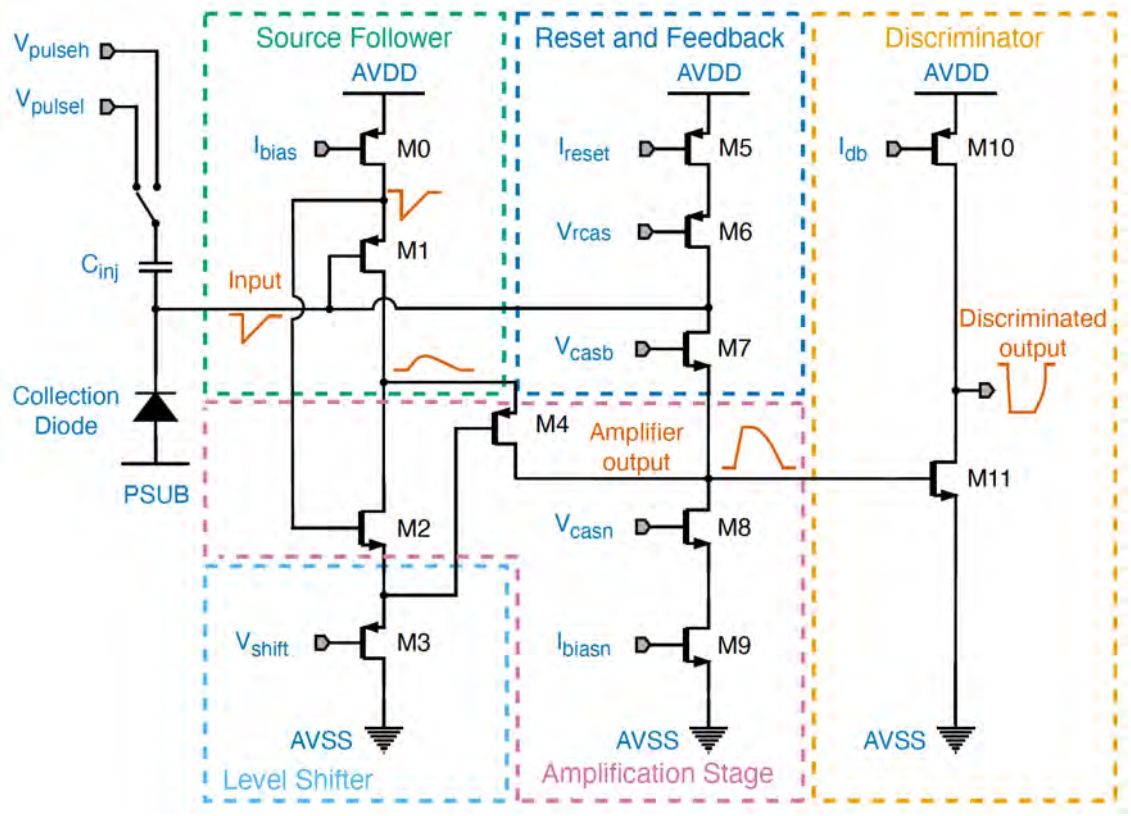


Figure A.1: Simplified schematic of in-pixel front-end circuit. Taken from [17].

```
[RunControl]
EUDAQ_CTRL_PRODUCER_LAST_START = MOSSRAISER_3
EUDAQ_CTRL_PRODUCER_FIRST_STOP = MOSSRAISER_3
NEVENTS = 100000

[Producer.PTH_0]
EUDAQ_DC = dc

[Producer.POWER_0]
EUDAQ_DC = dc

[Producer.POWER_1]
EUDAQ_DC = dc

[Producer.MOSSRAISER_0]
EUDAQ_DC = dc
EUDAQ_ID = 0
STROBE_LENGTH = 200
tb_region0_VCASB = 15
tb_region1_VCASB = 15
tb_region2_VCASB = 20
tb_region3_VCASB = 15
bb_region0_VCASB = 15
bb_region1_VCASB = 15
bb_region2_VCASB = 15
bb_region3_VCASB = 12

[Producer.MOSSRAISER_1]
EUDAQ_DC = dc
EUDAQ_ID = 1
STROBE_LENGTH = 200
tb_region0_VCASB = 15
tb_region1_VCASB = 15
tb_region2_VCASB = 20
tb_region3_VCASB = 15
bb_region0_VCASB = 15
bb_region1_VCASB = 15
bb_region2_VCASB = 15
bb_region3_VCASB = 12
```

Listing A.1: Part of an EUDQ configuration file, displaying the V_{casb} values of the reference planes.

A.1 Detection Efficiency

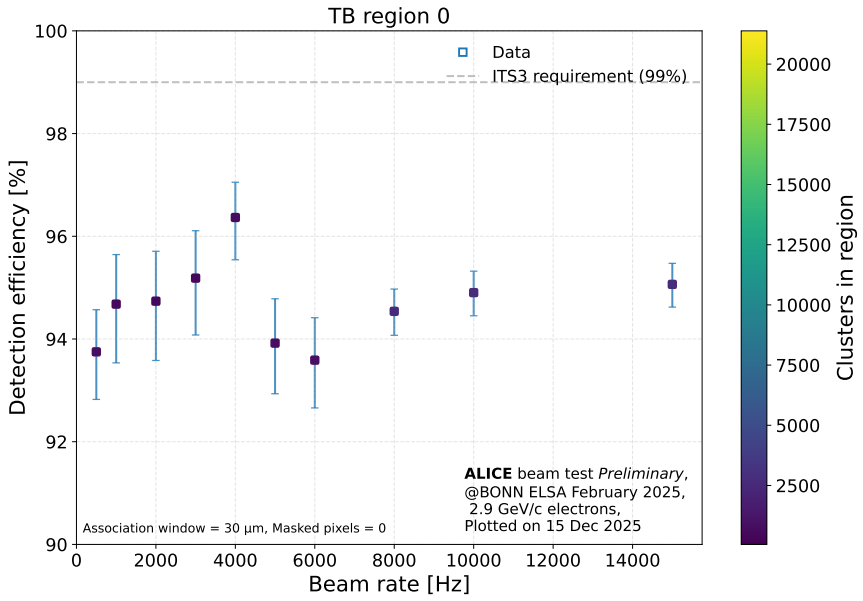


Figure A.2: Detection efficiency of top region 0 in dependence of the beam rate.

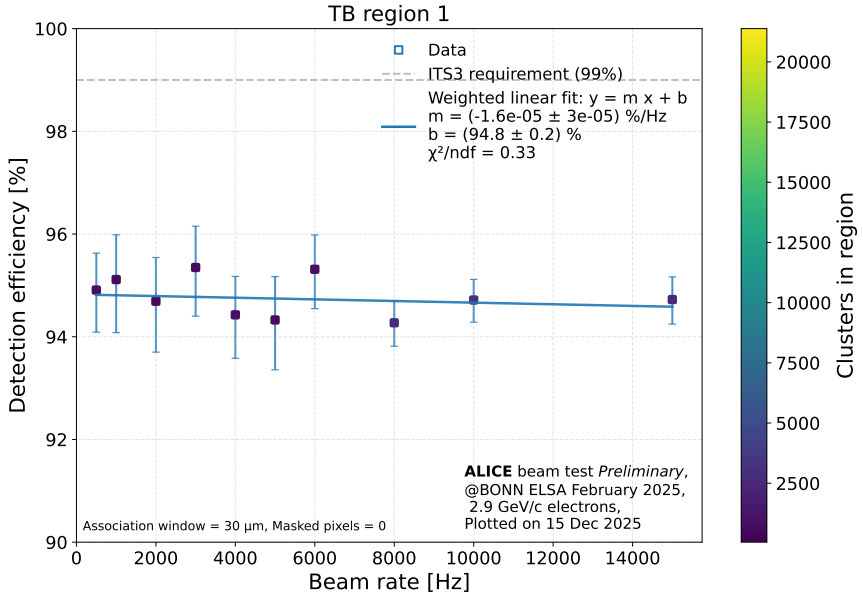


Figure A.3: Detection efficiency of top region 1 in dependence of the beam rate. The data was fitted with a linear function.

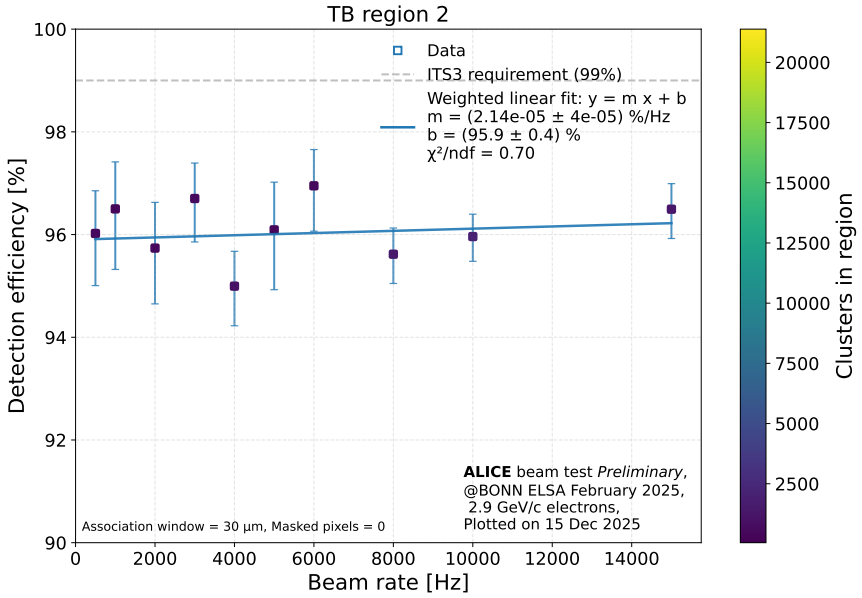


Figure A.4: Detection efficiency of top region 2 in dependence of the beam rate. The data was fitted with a linear function.

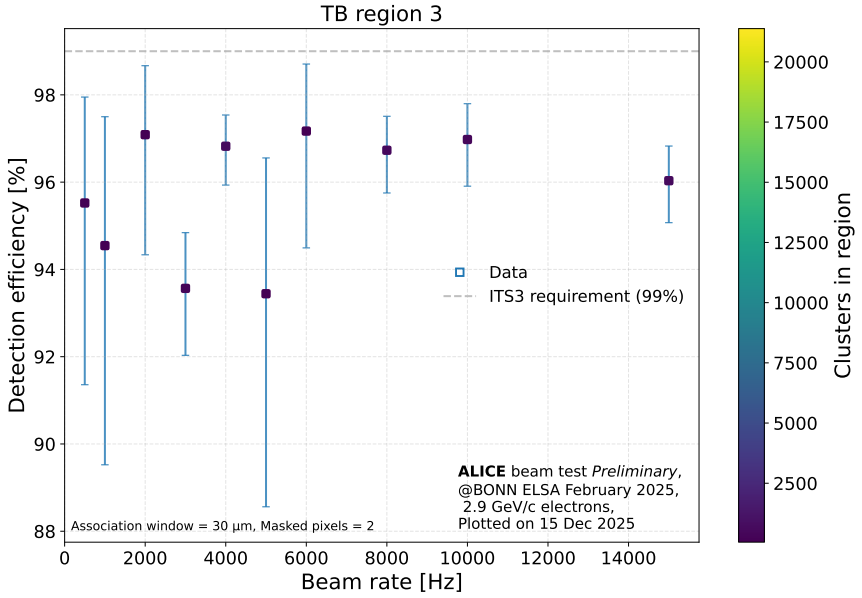


Figure A.5: Detection efficiency of top region 3 in dependence of the beam rate. The data was fitted with a linear function.

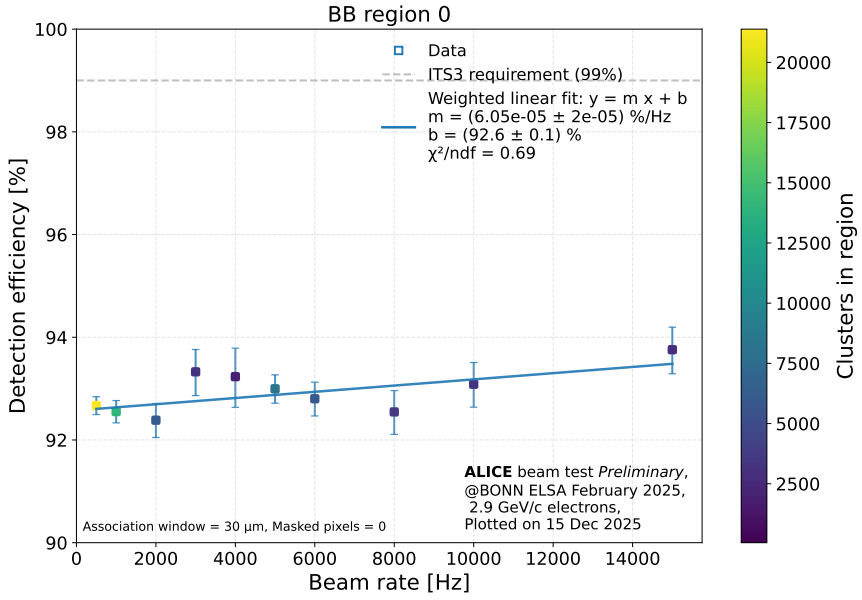


Figure A.6: Detection efficiency of bottom region 0 in dependence of the beam rate. The data was fitted with a linear function.

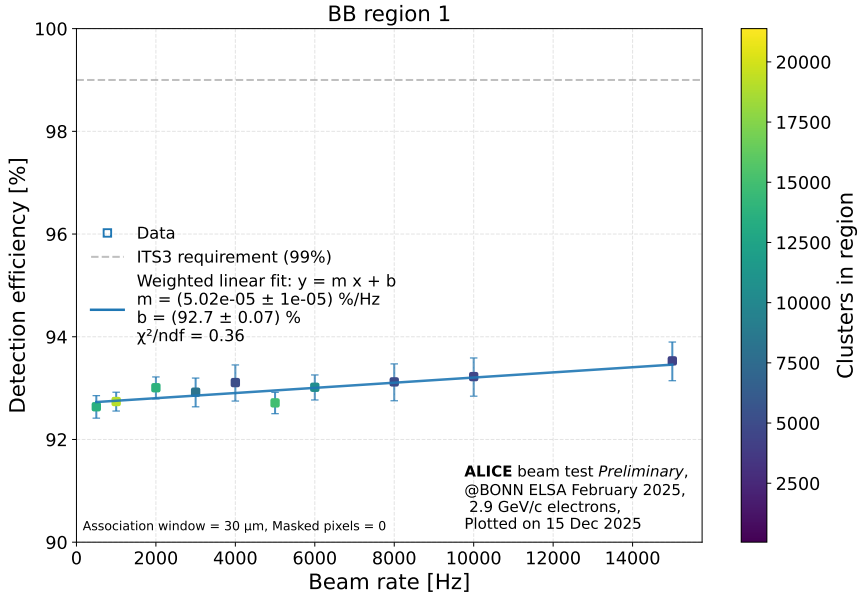


Figure A.7: Detection efficiency of bottom region 1 in dependence of the beam rate. The data was fitted with a linear function.

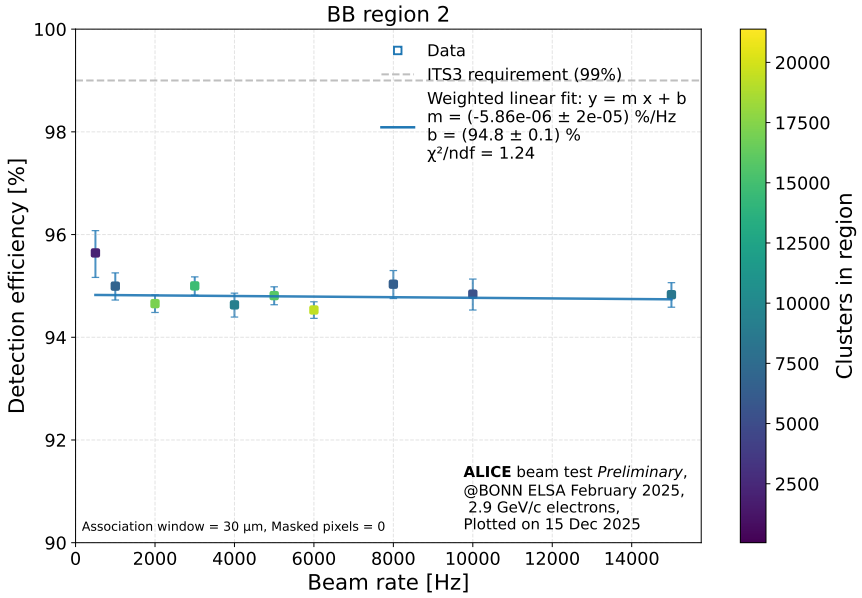


Figure A.8: Detection efficiency of bottom region 2 in dependence of the beam rate. The data was fitted with a linear function.

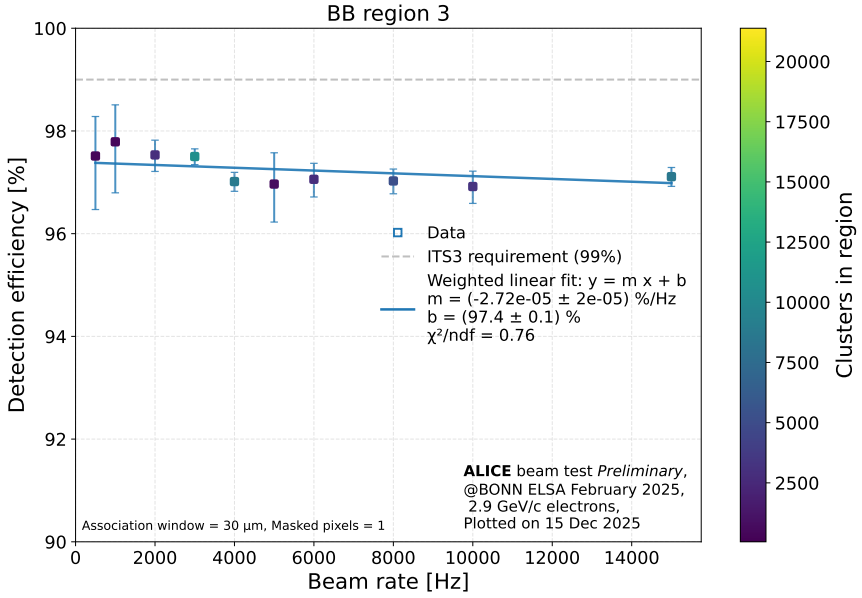


Figure A.9: Detection efficiency of bottom region 3 in dependence of the beam rate. The data was fitted with a linear function.

A.2 Spatial Resolution

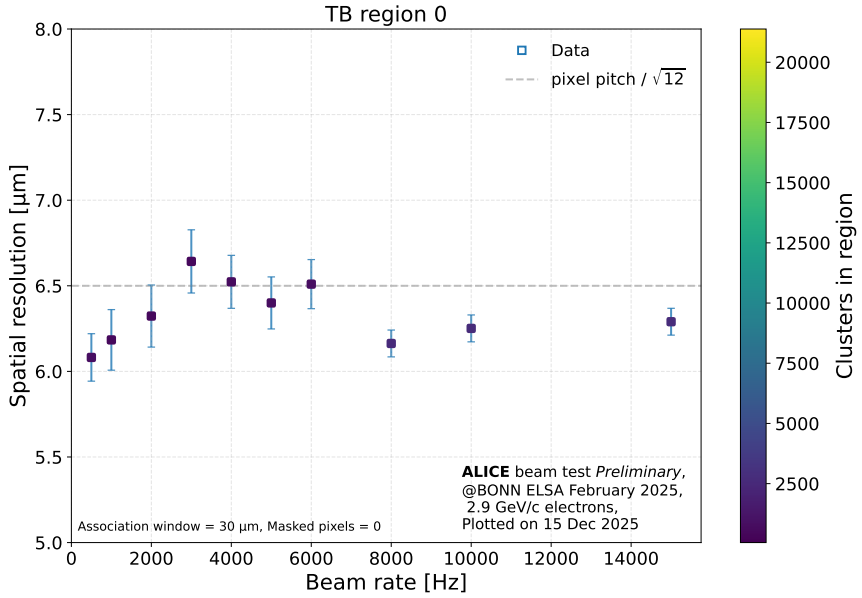


Figure A.10: Spatial resolution of top region 0 as a function of the beam rate for a representative bottom half-unit region.

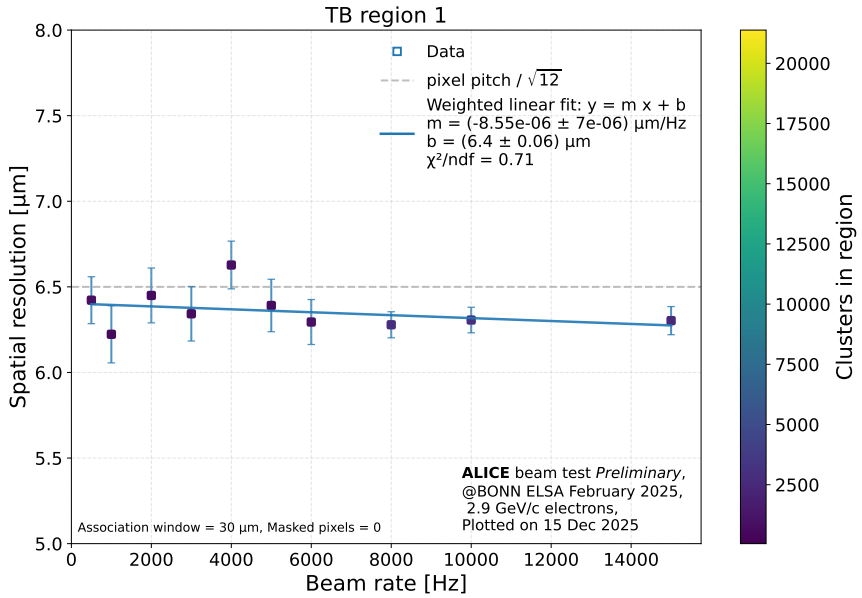


Figure A.11: Spatial resolution of top region 1 as a function of the beam rate for a representative bottom half-unit region. The data was fitted with a linear function.

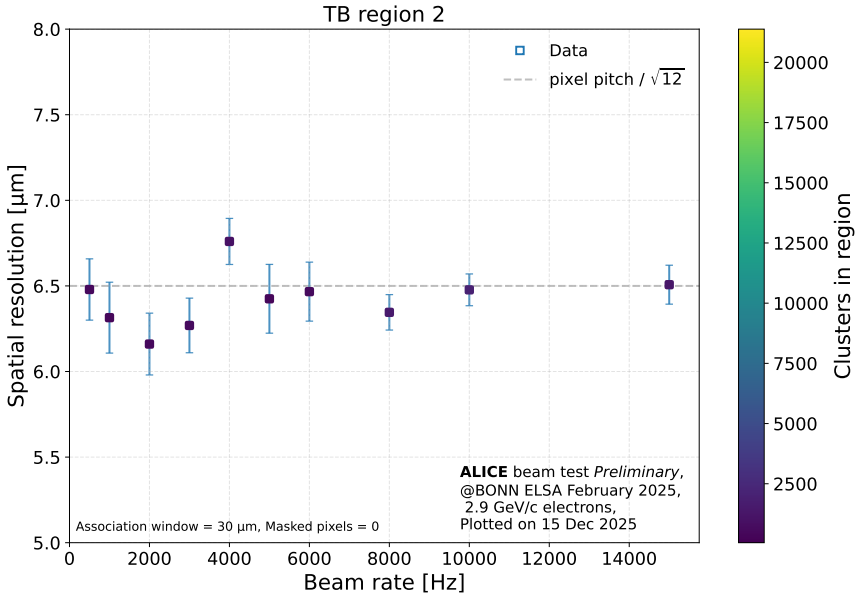


Figure A.12: Spatial resolution of top region 2 as a function of the beam rate for a representative bottom half-unit region.

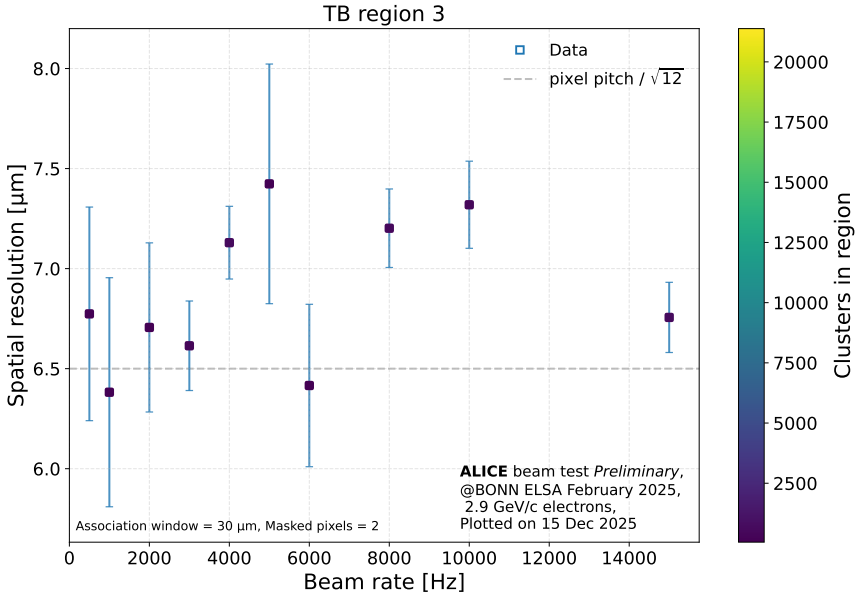


Figure A.13: Spatial resolution of top region 3 as a function of the beam rate for a representative bottom half-unit region.

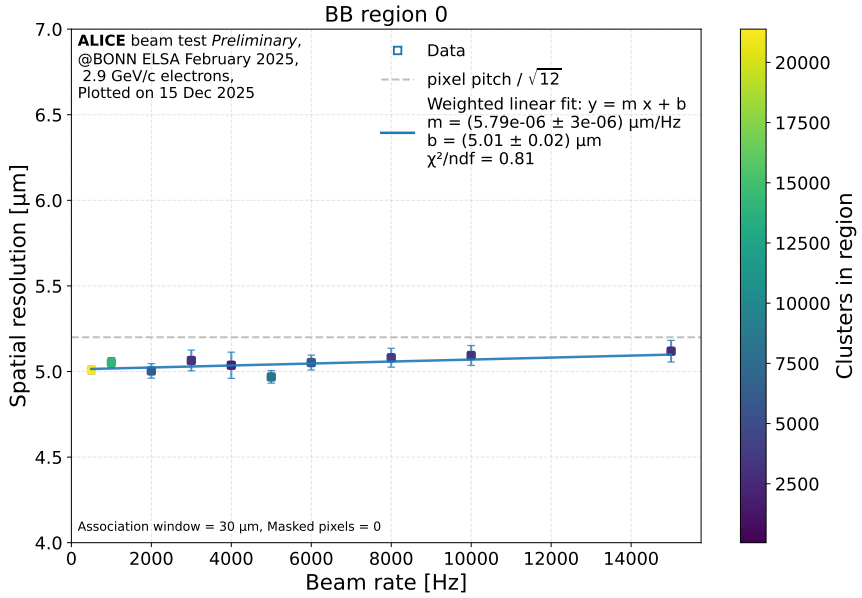


Figure A.14: Spatial resolution of bottom region 0 as a function of the beam rate for a representative bottom half-unit region. The data was fitted with a linear function.

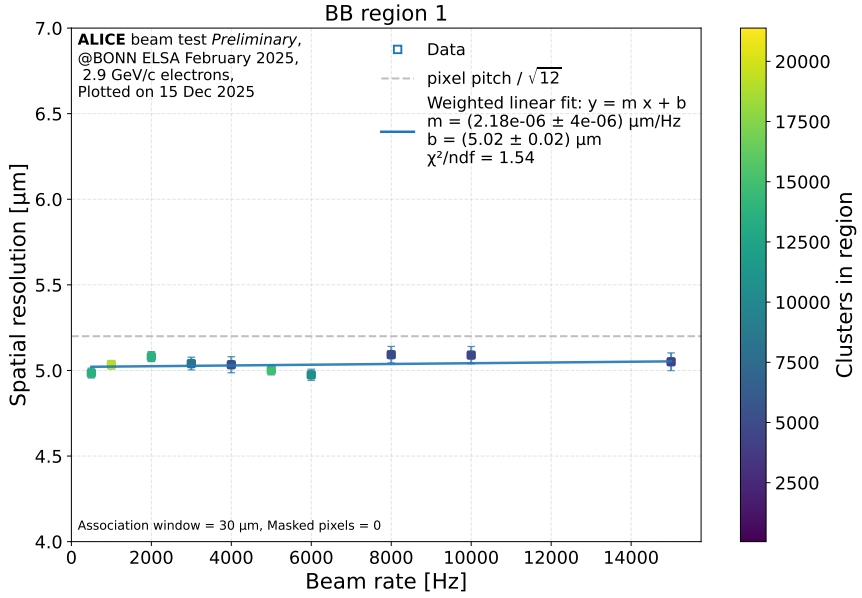


Figure A.15: Spatial resolution of bottom region 1 as a function of the beam rate for a representative bottom half-unit region. The data was fitted with a linear function.

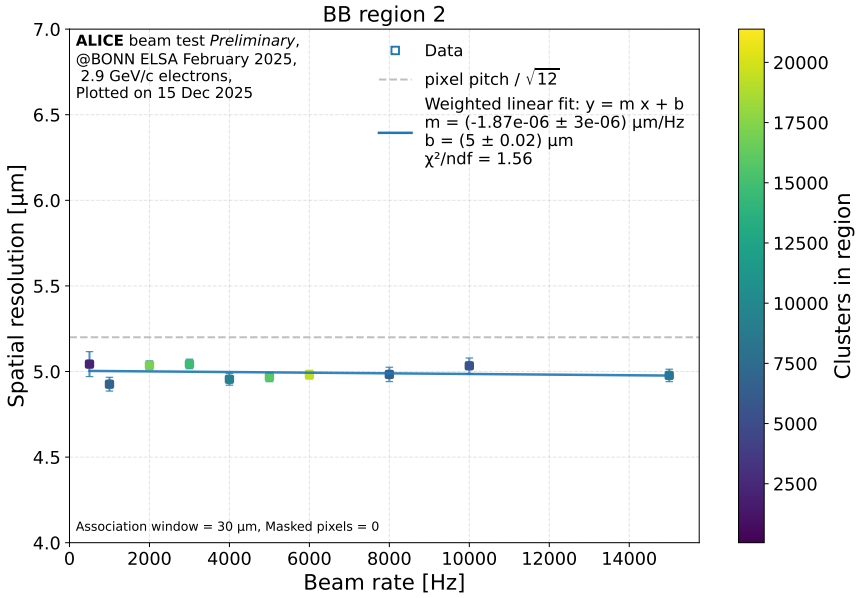


Figure A.16: Spatial resolution of bottom region 2 as a function of the beam rate for a representative bottom half-unit region. The data was fitted with a linear function.

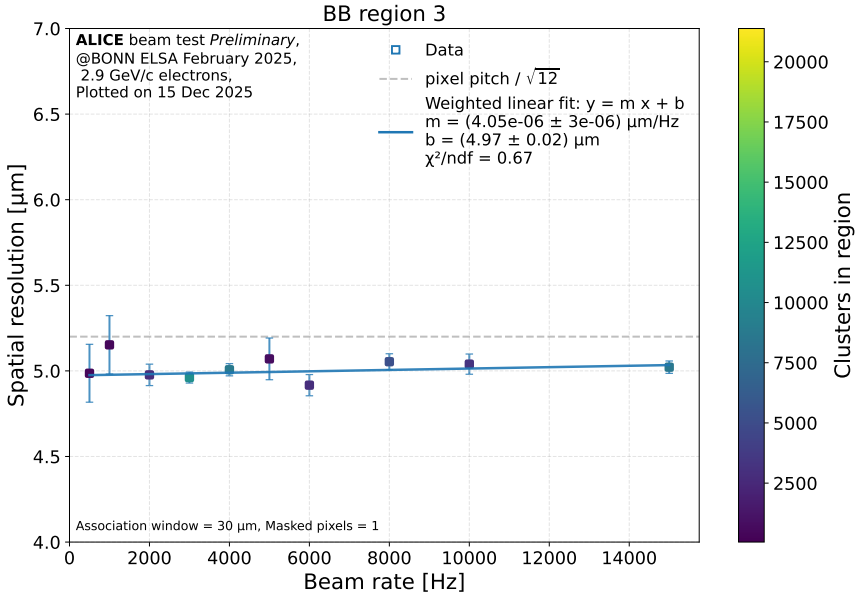


Figure A.17: Spatial resolution of bottom region 3 as a function of the beam rate for a representative bottom half-unit region. The data was fitted with a linear function.

A.3 FHR and THR scans

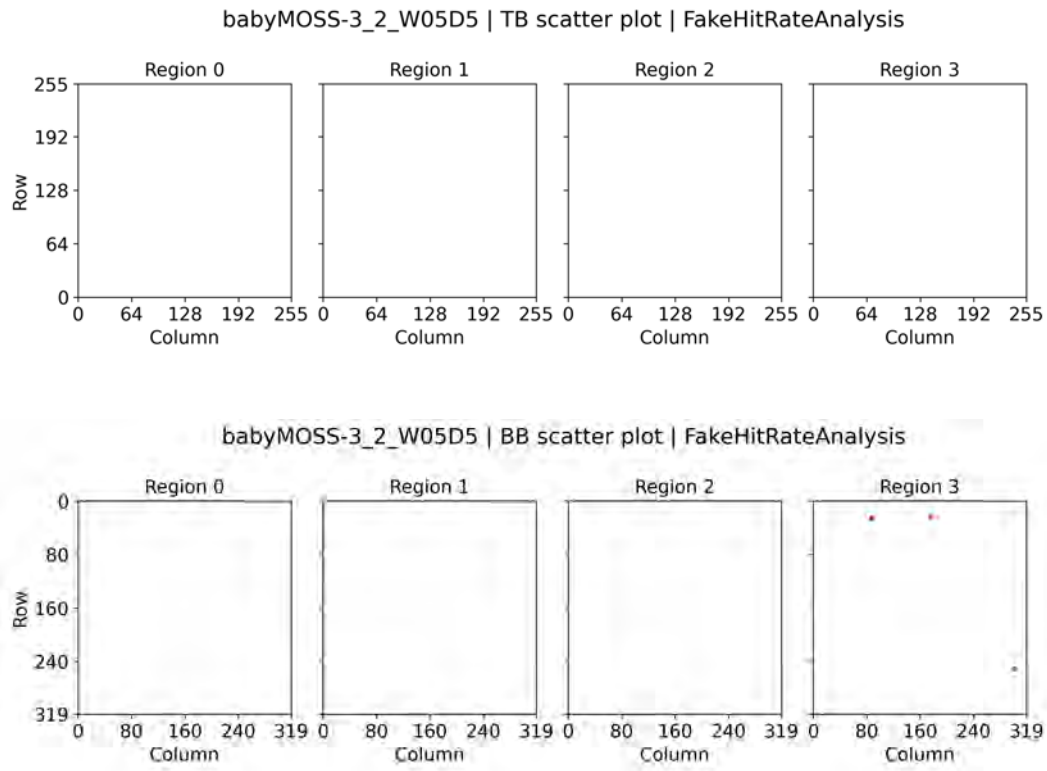


Figure A.18: Scatter plots of the FHR scan with $V_{psub} = -1.2\,V$ and from left to right and top to bottom $V_{casb} = (75,\ 75,\ 80,\ 75,\ 75,\ 75,\ 75,\ 70)\,\mathrm{DAC}$ units.

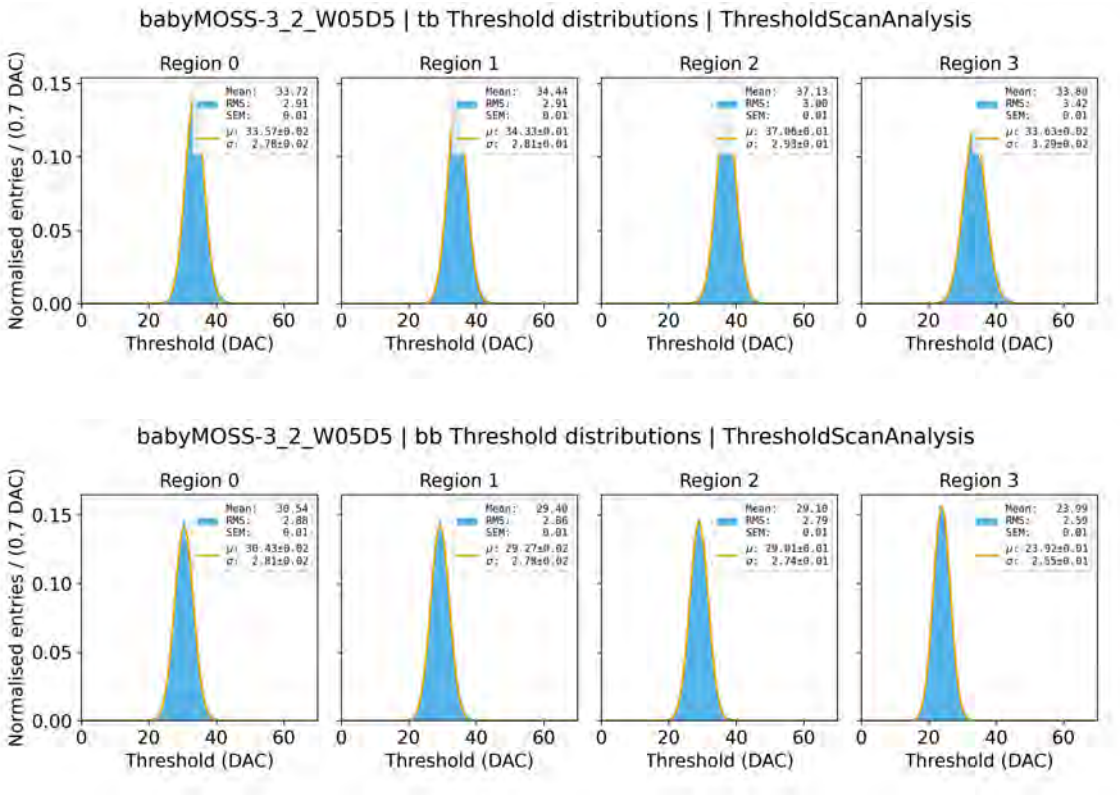


Figure A.19: Threshold distribution of the THR scan with babyMOSS standard settings $V_{casb} = 15\,\mathrm{DAC}$ units and $V_{psub} = 0\,\mathrm{V}$.

Table A.1: Spatial resolution, cluster size, detection efficiency, and number of clusters for each beam rate and region.

HU	Region	Spatial res. (μm)	Cluster size	Efficiency (%)	N_{cluster}
Beam rate: 500 Hz					
bb	0	5.055 ± 0.028	1.110	$92.67^{+0.17}_{-0.18}$	21381
bb	1	4.997 ± 0.034	1.116	$92.64^{+0.22}_{-0.22}$	13563
bb	2	4.794 ± 0.086	1.149	$95.64^{+0.43}_{-0.48}$	2129
bb	3	4.872 ± 0.300	1.171	$97.51^{+0.77}_{-1.04}$	392
tb	0	5.953 ± 0.198	1.109	$93.75^{+0.82}_{-0.93}$	825
tb	1	6.205 ± 0.191	1.092	$94.91^{+0.72}_{-0.82}$	895
tb	2	6.376 ± 0.276	1.115	$96.02^{+0.83}_{-1.02}$	531
tb	3	7.355 ± 1.860	1.078	$95.52^{+2.43}_{-4.16}$	64
Beam rate: 1000 Hz					
bb	0	5.039 ± 0.034	1.113	$92.55^{+0.21}_{-0.22}$	13982
bb	1	5.028 ± 0.029	1.121	$92.74^{+0.18}_{-0.19}$	19107
bb	2	4.917 ± 0.048	1.133	$95.00^{+0.26}_{-0.27}$	6815
bb	3	5.046 ± 0.291	1.161	$97.79^{+0.72}_{-0.99}$	398
tb	0	6.217 ± 0.292	1.107	$94.68^{+0.96}_{-1.14}$	516
tb	1	6.139 ± 0.257	1.080	$95.11^{+0.87}_{-1.03}$	584
tb	2	6.923 ± 0.418	1.104	$96.50^{+0.92}_{-1.18}$	386
tb	3	6.918 ± 2.165	1.115	$94.55^{+2.95}_{-5.02}$	52
Beam rate: 2000 Hz					
bb	0	4.813 ± 0.049	1.122	$92.39^{+0.28}_{-0.30}$	6212
bb	1	5.050 ± 0.062	1.120	$92.76^{+0.17}_{-0.18}$	13740
bb	2	4.933 ± 0.040	1.130	$94.50^{+0.13}_{-0.14}$	17108
bb	3	4.853 ± 0.055	1.168	$97.27^{+0.33}_{-0.41}$	2847
tb	0	5.934 ± 0.113	1.099	$94.65^{+0.48}_{-0.53}$	504
tb	1	6.153 ± 0.118	1.082	$95.00^{+0.44}_{-0.48}$	660
tb	2	6.471 ± 0.168	1.093	$95.78^{+0.47}_{-0.55}$	494

Continued on next page

HU	Region	Spatial res. (μm)	Cluster size	Efficiency (%)	N_{cluster}
tb	3	7.247 ± 0.565	1.080	$94.61^{+0.99}_{-1.38}$	100
Beam rate: 3000 Hz					
bb	0	4.959 ± 0.074	1.106	$93.33^{+0.41}_{-0.44}$	3091
bb	1	4.973 ± 0.062	1.118	$92.98^{+0.21}_{-0.23}$	8138
bb	2	4.905 ± 0.046	1.138	$94.81^{+0.18}_{-0.19}$	14708
bb	3	4.857 ± 0.056	1.170	$97.14^{+0.25}_{-0.31}$	10696
tb	0	5.986 ± 0.096	1.100	$94.11^{+0.48}_{-0.54}$	514
tb	1	6.256 ± 0.108	1.084	$94.82^{+0.44}_{-0.49}$	656
tb	2	6.615 ± 0.156	1.099	$95.69^{+0.50}_{-0.59}$	645
tb	3	7.072 ± 0.410	1.088	$94.90^{+0.76}_{-1.01}$	349
Beam rate: 4000 Hz					
bb	0	4.837 ± 0.090	1.095	$93.23^{+0.47}_{-0.50}$	1929
bb	1	4.954 ± 0.076	1.112	$93.06^{+0.27}_{-0.29}$	5093
bb	2	4.984 ± 0.052	1.127	$94.90^{+0.21}_{-0.22}$	9271
bb	3	4.885 ± 0.068	1.175	$97.24^{+0.28}_{-0.35}$	8774
tb	0	6.013 ± 0.097	1.103	$94.23^{+0.51}_{-0.58}$	716
tb	1	6.303 ± 0.110	1.088	$94.73^{+0.49}_{-0.55}$	898
tb	2	6.686 ± 0.165	1.107	$95.80^{+0.57}_{-0.68}$	987
tb	3	6.406 ± 0.284	1.140	$96.82^{+1.04}_{-1.50}$	579
Beam rate: 5000 Hz					
bb	0	4.947 ± 0.115	1.106	$93.25^{+0.52}_{-0.55}$	8273
bb	1	4.946 ± 0.093	1.119	$93.00^{+0.29}_{-0.30}$	14949
bb	2	5.000 ± 0.062	1.130	$94.90^{+0.21}_{-0.22}$	15841
bb	3	4.864 ± 0.076	1.170	$97.39^{+0.32}_{-0.40}$	767
tb	0	6.056 ± 0.102	1.104	$94.08^{+0.57}_{-0.65}$	726
tb	1	6.384 ± 0.117	1.089	$94.05^{+0.59}_{-0.68}$	715
tb	2	6.866 ± 0.189	1.100	$95.76^{+0.77}_{-0.96}$	418
tb	3	8.350 ± 2.318	1.070	$93.44^{+3.78}_{-5.55}$	57

Continued on next page

HU	Region	Spatial res. (μm)	Cluster size	Efficiency (%)	N_{cluster}
Beam rate: 6000 Hz					
bb	0	5.012 ± 0.142	1.108	$92.86^{+0.58}_{-0.62}$	6022
bb	1	4.981 ± 0.112	1.118	$92.75^{+0.33}_{-0.35}$	10549
bb	2	5.028 ± 0.078	1.127	$94.75^{+0.24}_{-0.25}$	19327
bb	3	4.853 ± 0.092	1.170	$97.30^{+0.39}_{-0.50}$	2871
tb	0	6.082 ± 0.116	1.104	$94.01^{+0.60}_{-0.69}$	832
tb	1	6.471 ± 0.141	1.088	$93.74^{+0.66}_{-0.78}$	956
tb	2	6.976 ± 0.239	1.096	$95.68^{+0.92}_{-1.17}$	572
tb	3	7.335 ± 1.289	1.136	$97.17^{+1.56}_{-2.39}$	103
Beam rate: 8000 Hz					
bb	0	4.998 ± 0.195	1.102	$92.44^{+0.62}_{-0.66}$	3725
bb	1	4.979 ± 0.145	1.112	$92.46^{+0.36}_{-0.38}$	4887
bb	2	4.992 ± 0.102	1.121	$94.60^{+0.28}_{-0.29}$	6391
bb	3	4.839 ± 0.120	1.173	$97.36^{+0.52}_{-0.68}$	5221
tb	0	6.111 ± 0.127	1.106	$94.18^{+0.47}_{-0.52}$	2614
tb	1	6.533 ± 0.149	1.094	$94.23^{+0.50}_{-0.56}$	2831
tb	2	7.151 ± 0.291	1.114	$95.62^{+0.66}_{-0.79}$	1549
tb	3	7.517 ± 0.358	1.127	$96.73^{+1.15}_{-1.66}$	503
Beam rate: 10000 Hz					
bb	0	4.937 ± 0.252	1.101	$92.14^{+0.70}_{-0.76}$	3379
bb	1	5.046 ± 0.216	1.104	$92.26^{+0.61}_{-0.66}$	4499
bb	2	5.182 ± 0.148	1.114	$94.78^{+0.54}_{-0.59}$	5422
bb	3	4.926 ± 0.233	1.180	$97.20^{+0.96}_{-1.34}$	3239
tb	0	6.394 ± 0.169	1.104	$94.37^{+1.03}_{-1.23}$	2644
tb	1	6.598 ± 0.170	1.106	$94.68^{+1.01}_{-1.20}$	2957
tb	2	7.015 ± 0.295	1.125	$96.35^{+1.29}_{-1.67}$	1972
tb	3	7.270 ± 0.393	1.126	$96.06^{+1.60}_{-2.49}$	417
Beam rate: 15000 Hz					

Continued on next page

HU	Region	Spatial res. (μm)	Cluster size	Efficiency (%)	N_{cluster}
bb	0	5.062 ± 0.286	1.098	$92.41^{+0.92}_{-1.00}$	2869
bb	1	4.999 ± 0.263	1.103	$92.54^{+0.76}_{-0.83}$	4236
bb	2	5.094 ± 0.215	1.112	$94.98^{+0.65}_{-0.70}$	8528
bb	3	4.670 ± 0.343	1.159	$97.09^{+1.07}_{-1.50}$	8569
tb	0	6.545 ± 0.245	1.103	$94.56^{+1.10}_{-1.31}$	2677
tb	1	6.604 ± 0.247	1.099	$94.62^{+1.14}_{-1.35}$	2442
tb	2	6.871 ± 0.379	1.118	$96.10^{+1.39}_{-1.79}$	1321
tb	3	6.602 ± 0.281	1.133	$96.03^{+1.11}_{-1.57}$	581

List of Figures

2.1 Schematical representation of energy band structure of isolators (a), semiconductors (b) and conductors (c,d). E_g is the width of the band gap in terms of energy. Taken and translated from [4, p. 278]. 5

2.2 Schematic illustration of a pn-junction, showing the depletion region and the internal electric field. Taken and modified from [4]. . . 6

2.3 Schematic visualization of the *ALPIDE* cross section. Taken and adapted from [7]. 8

3.1 Schematic overview of the ALICE 2 detector and its main subdetectors. Taken from [16] 14

3.2 Schematic wafermap with six MOSS in the center and 23 babyMOSS in the remaining space on the wafer. Taken from [18] 16

3.3 Photograph of a babyMOSS sensor mounted on its carrier PCB. Photograph taken by L. Halstenberg; Annotations by A. Rachev. 17

4.1 Schematic of a DESY-type telescope setup with six reference planes and one DUT. Taken from [8] 19

4.2 Photograph of the DAQ raiser Setup. From left to right: babyMOSS on carrier PCB, raiser board, DAQ board. Photograph by I. Panasenko. 21

4.3 Photograph of the beam telescope setup (side view) used in the February 2025 test beam. The main components are colour-coded and labelled, including the reference planes, scintillators, USB hub, and trigger board. The DUT is not installed. Photograph by I. Panasenko; Annotations by A. Rachev. 22

4.4 Schematic of the trigger chain of the babyMOSS telescope setup. Taken from [20]. 23

4.5 Schematic of the ELSA accelerator. Taken from [21]. 24

4.6 Photograph of the E3 beamline with two beam telescopes on the left and the and the beam pipe on the right. Surrounding the pipe are quadrupole magnet (yellow) and a dipole magnet (red). Photograph by L. Halstenberg. 26

4.7 Correlation of the hit positions along the x-axis for bb region 1, shown for the plane pairs (a) plane 0–plane 1 and (b) plane 0–plane 6. . . 27

4.8 Geometry file of one reference plane and the DUT plane. 28

4.9 Configuration file for the masking. 29

4.10 Configuration file for the prealignment. 30

4.11 Part of an alignment configuration file. Modules that were already shown in other configuration files are excluded from this graphic. . . 31

5.1 Hitmaps of the measurements with an approximated beam rate of $500\,\mathrm{Hz} - 2000\,\mathrm{Hz}$. Due to the different pixel pitch in top and bottom units the scale is altered resulting in an offset between top and bottom hitmaps. 35

5.2 Hitmaps of the measurements with an approximated beam rate of $3000\,\mathrm{Hz} - 5000\,\mathrm{Hz}$. Due to the different pixel pitch in top and bottom units the scale is altered resulting in an offset between top and bottom hitmaps. 36

5.3 Hitmaps of the measurements with an approximated beam rate of $6000\,\mathrm{Hz} - 10000\,\mathrm{Hz}$. Due to the different pixel pitch in top and bottom units the scale is altered resulting in an offset between top and bottom hitmaps. 37

5.4 Hitmap of the measurement with an approximated beam rate of $15000\,\mathrm{Hz}$. Due to the different pixel pitch in top and bottom units the scale is altered resulting in an offset between top and bottom hitmaps. . . . 38

5.5 Detection efficiency of bottom region 1 in dependence of the beam rate. The data was fitted with a linear function. 39

5.6 Detection efficiency of top region 2 in dependence of the beam rate. The data was fitted with a linear function. 39

5.7 Residual distributions in the y direction for regions with high (left) and low (right) statistics. 42

5.8 Spatial resolution of bottom region 1 as a function of the beam rate for a representative bottom half-unit region. The data was fitted with a linear function. 44
5.9 Spatial resolution of top region 1 as a function of the beam rate for a representative bottom half-unit region. The data was fitted with a linear function. 45
5.10 Reduced χ^2 of the fits for the tracks in bottom region 0 at $500\,\mathrm{Hz}$. . . 46

A.1 Simplified schematic of in-pixel front-end circuit. Taken from [17]. . 51
A.2 Detection efficiency of top region 0 in dependence of the beam rate. 53
A.3 Detection efficiency of top region 1 in dependence of the beam rate. The data was fitted with a linear function. 53
A.4 Detection efficiency of top region 2 in dependence of the beam rate. The data was fitted with a linear function. 54
A.5 Detection efficiency of top region 3 in dependence of the beam rate. The data was fitted with a linear function. 54
A.6 Detection efficiency of bottom region 0 in dependence of the beam rate. The data was fitted with a linear function. 55
A.7 Detection efficiency of bottom region 1 in dependence of the beam rate. The data was fitted with a linear function. 55
A.8 Detection efficiency of bottom region 2 in dependence of the beam rate. The data was fitted with a linear function. 56
A.9 Detection efficiency of bottom region 3 in dependence of the beam rate. The data was fitted with a linear function. 56
A.10 Spatial resolution of top region 0 as a function of the beam rate for a representative bottom half-unit region. 57
A.11 Spatial resolution of top region 1 as a function of the beam rate for a representative bottom half-unit region. The data was fitted with a linear function. 57
A.12 Spatial resolution of top region 2 as a function of the beam rate for a representative bottom half-unit region. 58
A.13 Spatial resolution of top region 3 as a function of the beam rate for a representative bottom half-unit region. 58

A.14 Spatial resolution of bottom region 0 as a function of the beam rate for a representative bottom half-unit region. The data was fitted with a linear function. 59
A.15 Spatial resolution of bottom region 1 as a function of the beam rate for a representative bottom half-unit region. The data was fitted with a linear function. 59
A.16 Spatial resolution of bottom region 2 as a function of the beam rate for a representative bottom half-unit region. The data was fitted with a linear function. 60
A.17 Spatial resolution of bottom region 3 as a function of the beam rate for a representative bottom half-unit region. The data was fitted with a linear function. 60
A.18 Scatter plots of the FHR scan with $\mathrm{V_{psub}} = -1.2\,\mathrm{V}$ and from left to right and top to bottom $\mathrm{V_{casb}} = (75,\ 75,\ 80,\ 75,\ 75,\ 75,\ 75,\ 70)\,\mathrm{DAC}$ units. 61
A.19 Threshold distribution of the THR scan with babyMOSS standard settings $\mathrm{V_{casb}} = 15\,\mathrm{DAC}$ units and $\mathrm{V_{psub}} = 0\,\mathrm{V}$. 62

List of Tables

5.1 Information about the DUT that was used and the settings it ran with during all measurements. 33
5.2 Average detection efficiency per region, averaged over all beam rates. 41
5.3 Input parameters used for the Telescope Optimizer. 43

A.1 Spatial resolution, cluster size, detection efficiency, and number of clusters for each beam rate and region. 63

Bibliography

[1] Christian Klein-Bösing. “Study of the Quark-Gluon Plasma with Hard and Electromagnetic Probes”. Habilitation thesis. Westfälische Wilhelms-Universität Münster, 2013.

[2] ALICE Collaboration. *ALICE ITS Upgrade Technical Design Report*. CERN-LHCC-2024-003. CERN, 2024.

[3] ALICE Collaboration. *Letter of Intent for ALICE 3: A Next-Generation Heavy-Ion Experiment at the LHC*. CERN-LHCC-2022-009. CERN, 2022. arXiv: 2211.02491.

[4] Hermann Kolanoski and Norbert Wermes. *Teilchendetektoren: Grundlagen und Anwendungen*. Berlin, Heidelberg: Springer, 2016.

[5] K. A. Olive et al. “Review of Particle Physics”. In: *Chinese Physics C* 38.9 (2014). DOI: 10.1088/1674-1137/38/9/090001.

[6] Nicolas Tiltmann. “Radiation Hardness of Digital Pixel Sensor Prototypes in 65 nm CMOS Technology for the ALICE ITS3 Upgrade”. Supervisors: A. Andronic and C. Klein-Bösing. Master’s Thesis. Westfälische Wilhelms-Universität Münster, Sept. 2023.

[7] Isabella Sanna. “Development and Performance Study for the ALICE ITS3”. PhD thesis. Technische Universität München, 2024.

[8] Hendrik Jansen et al. “Performance of the EUDET-type beam telescopes”. In: *The European Physical Journal C* 76.9 (2016). DOI: 10.1140/epjc/s10052-016-4450-7.

[9] R. Frühwirth. “Application of Kalman filtering to track and vertex fitting”. In: *Nuclear Instruments and Methods in Physics Research Section A* 262 (1987). DOI: 10.1016/0168-9002(87)90887-4.

[10] R. Frühwirth and A. Strandlie, eds. *Track Reconstruction and Pattern Recognition in Particle Physics*. Vol. 260. Springer Tracts in Modern Physics. Springer, 2013. DOI: 10.1007/978-3-642-39290-4.

[11] Claus Kleinwort. "General Broken Lines as advanced track fitting method". In: *Nuclear Instruments and Methods in Physics Research Section A* 673 (2012). DOI: 10.1016/j.nima.2012.01.024.

[12] ATLAS Collaboration. "The ATLAS Experiment at the CERN Large Hadron Collider". In: *Journal of Instrumentation* 3.08 (2008), S08003. DOI: 10.1088/1748-0221/3/08/S08003.

[13] CMS Collaboration. "The CMS Experiment at the CERN LHC". In: *Journal of Instrumentation* 3.08 (2008), S08004. DOI: 10.1088/1748-0221/3/08/S08004.

[14] LHCb Collaboration. "The LHCb Detector at the LHC". In: *Journal of Instrumentation* 3.08 (2008), S08005. DOI: 10.1088/1748-0221/3/08/S08005.

[15] ALICE Collaboration. "The ALICE Experiment at the CERN LHC". In: *Journal of Instrumentation* 3.08 (2008), S08002. DOI: 10.1088/1748-0221/3/08/S08002.

[16] ALICE Collaboration. "Performance of the ALICE Experiment at the CERN LHC". In: *arXiv:1402.4476* (2014). Preprint. DOI: 10.48550/arXiv.1402.4476. arXiv: 1402.4476 [nucl-ex]. URL: https://arxiv.org/abs/1402.4476.

[17] Omar Abdelrahman et al. *Characterisation of the first wafer-scale prototype for the ALICE ITS3 upgrade: the monolithic stitched sensor (MOSS)*. 2025. arXiv: 2510.11463 [physics.ins-det]. URL: https://arxiv.org/abs/2510.11463.

[18] ALICE ITS3 Collaboration. *MOSS User Manual*. Internal documentation, CERN GitLab Wiki. 2024. URL: https://gitlab.cern.ch/groups/alice-its3-wp3/moss-testing/-/wikis/Moss%20user%20manual (visited on 02/14/2026).

[19] Alexander Rachev. "Commissioning of a babyMOSS beam telescope at the ELSA E3 beam line and sensor assembly for the ALICE3 experiment". MA thesis. Rheinischen Friedrich-Wilhelms-Universität Bonn, July 2025.

[20] Iaroslav Panasenko. *babyMOSS Telescope for ALICE ITS3 Pixel Sensor Characterization*. Presentation at the 13th Beam Telescopes and Test Beams Workshop. On behalf of the ALICE Collaboration. CERN, May 20, 2024.

[21] ROOT Collaboration. *ELSA Setup*. CERN. 2025. URL: https://www.pi.uni-bonn.de/elsa/de/beschleuniger/aufbau (visited on 02/10/2026).

[22] *The CBELSA/TAPS Experiment*. Physikalisches Institut, Rheinische Friedrich-Wilhelms-Universität Bonn. URL: https://www.cb.uni-bonn.de/ (visited on 02/10/2026).

[23] *The BGO-OD Experiment*. Physikalisches Institut, Rheinische Friedrich-Wilhelms-Universität Bonn. URL: https://www.pi.uni-bonn.de/bgood/en (visited on 02/10/2026).

[24] Dennis Proft et al. *The Detector Test Beamline at ELSA*. Presentation. Telescopes and Test Beams Workshop. 2021. URL: https://indico.cern.ch/event/945675/contributions/4160463/attachments/2186042/3693649/bttb21_elsa_testbeam.pdf.

[25] Dennis Proft. *Electron Stretcher Facility ELSA – Beam at the E3 Beamline*. Presentation. 2026. URL: https://indico.cern.ch/event/1640005/attachments/3209624/5716551/ELSA%20-%20Introduction.pdf.

[26] P. Ahlburg et al. "EUDAQ—a data acquisition software framework for common beam telescopes". In: *Journal of Instrumentation* 15.01 (Jan. 2020), P01038–P01038. ISSN: 1748-0221. DOI: 10.1088/1748-0221/15/01/p01038. URL: http://dx.doi.org/10.1088/1748-0221/15/01/P01038.

[27] Jens Kröger, Simon Spannagel, and Morag Williams. *User Manual for the Corryvreckan Test Beam Data Reconstruction Framework, Version 1.0*. 2019. arXiv: 1912.00856 [physics.ins-det]. URL: https://arxiv.org/abs/1912.00856.

[28] Volker Blobel, Claus Kleinwort, and Frank Meier. "Fast alignment of a complex tracking detector using advanced track models". In: *Computer Physics Communications* 182.9 (Sept. 2011), pp. 1760–1763. ISSN: 0010-4655. DOI: 10.1016/j.cpc.2011.03.017. URL: http://dx.doi.org/10.1016/j.cpc.2011.03.017.

[29] ROOT Collaboration. *TEfficiency Class Reference*. CERN. 2025. URL: https://root.cern.ch/doc/master/classTEfficiency.html (visited on 02/10/2026).

[30] JCGM. *Evaluation of measurement data – Guide to the expression of uncertainty in measurement*. JCGM 100:2008. Sèvres, France: Joint Committee for Guides in Metrology (JCGM), 2008.

[31] Magnus Mager. *Telescope Optimizer*. CERN. 2016. URL: https://mmager.web.cern.ch/telescope/tracking.html (visited on 02/14/2026).